Accepted Manuscript

Journal of the Geological Society

Igneous layering and magma dynamics in alkaline intrusions: textural evidence for gravitational settling and compaction within cumulates

Emily Jones, William McCarthy, Craig Magee, Tobias Mattsson, Sandra Piazolo, William Hutchison & Madeleine C.S. Humphreys

DOI: https://doi.org/10.1144/jgs2024-181

To access the most recent version of this article, please click the DOI URL in the line above. When citing this article please include the above DOI.

Received 6 September 2024
Revised 30 January 2025
Accepted 4 April 2025

Supplementary material at https://doi.org/10.6084/m9.figshare.c.7618284

Igneous layering and magma dynamics in alkaline intrusions: textural evidence for gravitational settling and compaction within cumulates

Abbreviated title: Igneous layering in alkaline intrusions

Emily Jones[1*], William McCarthy[1], Craig Magee[2], Tobias Mattsson[3], Sandra Piazolo[2], William Hutchison[1], Madeleine C.S. Humphreys[4]

[1] School of Earth and Environmental Sciences, University of St Andrews, KY16, 9TS, UK

[2] School of Earth and Environment, University of Leeds, LS2 9JT, UK

[3] Department of Earth Sciences, Uppsala University, Uppsala, 752 36, Sweden

[4] Department of Earth Sciences, Durham University, Durham, DH1 3LE, UK

ORCID ID: EJ, 0009-0002-4086-5845; WM, 0000-0002-7214-1449; CM, 0000-0001-9836-2365; TM, 0000-0003-0717-4014; SP, 0000-0001-7723-8170; WH, 0000-0002-5456-3277; MH, 0000-0001-9343-1237

*Corresponding author. E-mail: em208@st-andrews.ac.uk

Abstract

Mechanisms responsible for igneous layering and the concentration of critical minerals within alkaline intrusions remain debated. The Ilímaussaq complex, South Greenland, is a layered alkaline intrusion containing economically important rare earth element (REE) deposits. Based on geochemical and petrological data, the two leading hypotheses for the formation of igneous layering at Ilímaussaq are: (1) repeated magma recharge and in situ nucleation of minerals; or (2) gravitational settling of crystal mats within a closed magmatic system. We provide novel field, rock magnetic, and crystallographic preferred orientation (CPO) data from two representative outcrops of igneous layering at Ilímaussaq to test these hypotheses. Our rock magnetic data show that both arfvedsonite and magnetite contribute to the anisotropy of magnetic susceptibility (AMS) fabrics, with magnetite defining a sub-vertical foliation across igneous layering. Our data show that the AMS fabric is inverse to the silicate fabric (i.e. the magnetic foliation is normal to the silicate foliation), and records consistent sub-horizontal mineral foliations and lineations vertically through the layers. Critically, the silicate fabric is often oblique in both strike and dip to the modal igneous layering. Our measured fabrics best support a closed system crystal mat model and subsequent phases of differential and intrusion-wide compaction.

Supplementary material: Two supplementary figures are available at http://doi.org/10.17632/7xcf2cpr7g.2

Layered igneous intrusions preserve detailed records of the physical and chemical processes within magma reservoirs (e.g., Irvine, 1980; Tait and Jaupart, 1992; Naslund and McBirney, 1996; Namur et al., 2015; Nielsen et al., 2015; Latypov et al., 2017; O'Driscoll and Van Tongeren, 2017; Smith and Maier, 2021). To date, the vast majority of studies have focussed on layered intrusions that are mafic to ultramafic in composition (e.g., Boudreau and McBirney, 1997a; O'Driscoll et al., 2008; Holness et al., 2012, 2017; Nielsen et al., 2015; Latypov et al., 2017; Vukmanovic et al., 2019). Yet even for well-studied layered intrusions, such as Stillwater [USA], Bushveld [South Africa], Skaergaard [Greenland], and Rum [Scotland], their complex petrography means there is often a lack of consensus on how igneous layering formed (e.g., Boudreau, 1988; Eales & Cawthorn, 1996; Latypov et al., 2017; O'Driscoll et al., 2008; Smith & Maier, 2021). In contrast, alkaline layered intrusions, which can host important economic rare earth element (REE) deposits within their layers, have scarcely been investigated (e.g., Marks and Markl, 2015; Hunt et al., 2017; Borst et al., 2018; O'Driscoll et al., 2024). Exploring and targeting such REE deposits requires an in-depth understanding of the geological environments and processes that concentrate REEs within alkaline layered intrusions.

The origins of layering in igneous intrusions have primarily been studied using geochemical and mineralogical approaches (e.g., Borst et al., 2018; Duchesne & Charlier, 2005; Pang et al., 2009). However, these data are often ambiguous when interpreting the dominant layering mechanisms (e.g., Boorman et al., 2004). An alternative approach is to quantify the igneous textures, particularly the orientation and alignment of crystal phases (i.e. petrofabrics) (e.g., Branagan, 2005; O'Driscoll et al., 2008, 2015). These data enable us to quantitatively decipher crystallisation history, magma reservoir processes, and tectonic activity within igneous systems (e.g., Branagan, 2005; O'Driscoll et al., 2008; Petronis et al., 2012; Biedermann et al., 2016; Holness et al., 2017; O'Driscoll and Van Tongeren, 2017; Holness, 2018; Mattsson et al., 2021). However, due to exposure, grain size, and crystalline texture, identifying fabrics within igneous rocks is often difficult in the field. Anisotropy of magnetic susceptibility (AMS) provides a means of measuring magnetic fabrics, even when meso-to-macroscopic fabrics are not visible, in a fast, non-destructive, and three-dimensional manner (e.g., Borradaile, 1988; Knight and Walker, 1988; Tarling and Hrouda, 1993; Dunlop and Özdemir, 1997; Borradaile and Jackson, 2004; O'Driscoll et al., 2015; Bilardello, 2016; Magee et al., 2016; Koopmans et al., 2022). AMS functions as a tool for recording petrofabrics as most minerals are magnetically anisotropic; i.e. they are easier to magnetise in certain orientations depending on their crystallography and grain shape (e.g., Borradaile and Jackson, 2004; Martín-Hernández et al., 2004; O'Driscoll et al., 2008).

Here, we examine the Ilímaussaq complex, a layered alkaline intrusion located in South Greenland (e.g., Andersen et al., 1981; Bailey et al., 2001; Sørensen, 2001; Upton, 2013a; Marks and Markl, 2015). Ilímaussaq was emplaced at ~1.2 Ga as part of the Gardar alkaline province, and is of particular interest because its layered suite hosts world-class ore deposits containing REE, Zr, Nb, Hf, Ta, U, Li, Be, Zn and Th (e.g., Bailey et al., 2001; Borst et al., 2018; Larsen & Sørensen, 1987; Schønwandt et al., 2016; Sørensen, 2001; Sørensen et al., 2011). Two competing models have been proposed to explain the layering at Ilímaussaq: one model involves pulsed magmatic injection and in situ crystallisation in an open system environment (Hunt et al., 2017), whereas the other invokes crystal mat formation and gravitational settling in a closed system (Bons et al., 2015; Marks and Markl, 2015; Lindhuber et al., 2015; Borst et al., 2018). Recent work on a small suite of samples from Ilímaussaq demonstrated that AMS accurately records fabrics in the highly evolved nepheline syenites (O'Driscoll et al., 2024). We provide the first comprehensive field and rock magnetic study of several layer packages at Ilímaussaq, with exceptionally high spatial resolution, to test the open and closed system layering hypotheses. We show that the rock fabric best supports the latter hypothesis where layers form through crystal mats, in combination with compaction of the crystal mush which modifies the layering.

Geological Setting

<u>The Ilímaussaq complex</u>

The Ilímaussaq complex is a layered peralkaline (molar (Na + K)/Al > 1)) intrusion within the Gardar igneous province of South Greenland, which formed during two continental rifting events associated with the 1300–1100 Ma breakup of the Columbia/Nuna supercontinent (**Fig. 1**) (e.g., Upton et al., 2003; Marks et al., 2011; Upton, 2013; Marks and Markl, 2015). Ilímaussaq is ~17 x 8 km and oval shaped in map-view. It was emplaced at ~3–4 km depth between the granitic Julianehåb batholith (c. 1800 Ma) and overlying terrestrial sandstones and lavas of the Eriksfjord Formation (c. 1300–1270 Ma) (Garde et al., 2002; Krumrei et al., 2006; Upton, 2013b). Magmatic intrusion occurred between 1155–1165 Ma and the melt-mush system was likely active for ~1 Ma (Krumrei et al., 2006; Borst et al., 2019). No evidence of post-emplacement deformation has been recorded at Ilímaussaq making it an ideal natural laboratory to investigate primary alkaline magmatic processes (Upton et al., 2003; Upton, 2013b; Marks and Markl, 2015).

Ilímaussaq is famous for its mineral layering and chemically evolved mineralogy, as well as for hosting two world-class ore deposits, Kvanefjeld and Kringlerne, which contain ~1 billion and ~4.5 billion tonnes of total rare earth oxide (TREO), U and Zn, and TREO, Zr and Nb mineralisation, respectively (**Fig. 1**) (Sørensen, 2001; Borst et al., 2016; Schønwandt et al., 2016). Ilímaussaq formed through the emplacement of at least four magma batches: 1) an initial batch of augite syenite, which occurs around the perimeter of the complex; 2) a peralkaline granite and quartz syenite, which occur in the roof of the complex; 3) peralkaline nepheline syenites, which also occur within the roof horizon; and 4) a separate batch of peralkaline nepheline syenites that comprises the floor and 'sandwich' horizons (**Fig. 1**) (e.g., Borst et al., 2018; Pfaff et al., 2008; Ratschbacher et al., 2015; Sørensen et al., 2006). The nepheline syenites are the most well-studied part of the complex as they display significant layering and host the REE deposits (e.g., Bailey et al., 2001; Borst et al., 2018; Hunt et al., 2017; Sørensen, 2001). Within the nepheline syenites, the roof and 'sandwich' horizons are locally referred to as naujaite and lujavrite respectively (**Fig. 1**). The floor horizon, locally referred to as kakortokite (**Fig. 1**), is the focus of our study as it displays the most well-defined igneous layering.

The kakortokites are divided into three sequences (**Fig. 1a**); the >220 m thick lower layered kakortokites, slightly layered kakortokites and transitional layered kakortokites (e.g., Bohse et al., 1971; Borst et al., 2018; Marks & Markl, 2015). The focus of our study is on the lower layered kakortokites, which display well-defined layers, comprising two layering types: (1) an ~8 m thick three-layer unit, characterised by variations in modal abundances of arfvedsonite (inosilicate, monoclinic), eudialyte (cyclosilicate, trigonal), alkali feldspar (tectosilicate, monoclinic/triclinic), and nepheline (tectosilicate, hexagonal); and (2) the repetition of this three-layer unit a minimum of 29 times throughout the sequence (e.g., Bohse et al., 1971; Hunt et al., 2017; Marks & Markl, 2015; Sørensen, 2001). Each three-layer unit typically contains a black (B) arfvedsonite-rich layer at its base, a red (R) eudialyte group mineral (EGM)-rich layer in the centre, and a white (W) alkali feldspar- and nepheline-rich layer at the top; some units do not contain a red EGM-rich layer (Bohse et al., 1971). Each three-layer unit has been labelled -11 to +17, with respect to Unit 0 which is commonly accepted as the most well-developed three-layer unit in the sequence (e.g., Bohse et al., 1971; Borst et al., 2018; Hunt et al., 2017; Sørensen, 2001). The layered Unit +3 contains roof rock autoliths that layers above and below deflect around (**Fig. 1**) (e.g., Andersen et al., 1981; Bohse et al., 1971).

<u>Current models for the formation of kakortokite layering</u>

Models for layering in the Ilímaussaq kakortokites can be divided into two main groups: those supporting an open magmatic system with magma replenishment events, and those involving layer formation within a closed magmatic system (e.g., Larsen and Sørensen, 1987; Pfaff et al., 2008; Marks and Markl, 2015; Lindhuber et al., 2015; Hunt et al., 2017; Borst et al., 2018). In the most recently proposed open system model, Hunt et al. (2017) use EGM geochemistry and log-linear CSD data from arfvedsonite and eudialyte in Unit 0, to suggest in situ nucleation and growth of the black and red layers (**Fig. 2a**). In this open system model, an injection of a relatively primitive magma pools on the reservoir floor, where high concentrations of halogens inhibit the nucleation of all mineral phases except for arfvedsonite, which crystallises in situ to form the black layer (**Fig. 2a**) (Hunt et al., 2017).

As halogens transfer from the injected magma into the overlying residual magma, eudialyte becomes stable and crystalises in situ to form the red layer (**Fig. 2a**) (Hunt et al., 2017). Cooling of the injected magma leads to its thermal equilibration with the resident magma, and alkali feldspar and nepheline begin to nucleate, both in situ and suspended in the newly mixed magma, forming the white layer (**Fig. 2a**) (Hunt et al., 2017). Repetition of these three-layer units are suggested to represent new magma replenishment events with minimal compositional variations (Hunt et al., 2017).

Alternatively, a closed system model has been suggested where crystal mat formation is the main layering mechanism within the kakortokites (**Fig. 2b**) (Bons et al., 2015; Marks and Markl, 2015; Lindhuber et al., 2015; Borst et al., 2018). In this closed system model, cumulate minerals nucleate and grow below a rising crystallisation front and heavier minerals, such as arfvedsonite and eudialyte, sink whilst lighter minerals, such as alkali feldspar, float (**Fig. 2b**) (Bons et al., 2015; Lindhuber et al., 2015; Borst et al., 2018). As crystallisation continues, larger and heavier crystals catch up with smaller crystals sinking below them (i.e. hindered settling) and begin to form loosely aggregated mats (**Fig. 2b**) (Bons et al., 2015; Lindhuber et al., 2015). The crystal mats form progressively from the bottom of the magma reservoir upwards (Borst et al., 2018). With time the crystal mats grow and the acicular crystal habit of arfvedsonite forms dense mats and the more tabular habit of alkali feldspar forms looser, more porous mats (Lindhuber et al., 2015). Continued crystallisation, including the crystallisation of intercumulus material within the mats, forms quasi-closed mush systems (Bons et al., 2015; Marks and Markl, 2015; Lindhuber et al., 2015; Borst et al., 2018). Within these quasi-closed systems, internal melt fractionation and gravitational settling would further segregate the main cumulus minerals into three-layer units (**Fig. 2b**) (Bons et al., 2015; Lindhuber et al., 2015; Borst et al., 2018). While this closed system model is well supported by geochemical data, the in situ crystallisation recorded by CSD data, integral to the open system model, is at odds with the suggested gravitational settling.

<u>Predicted rock fabrics for existing layer formation hypotheses</u>

The competing hypotheses for the layering of the kakortokites hinge on mechanical processes that are expected to be reflected in rock fabric data (**Fig. 2 & 3**) (Meurer and Boudreau, 1998). Potential fabrics that may be observed are: (1) *mineral foliations* defined by the alignment of minerals along a plane; (2) *mineral lineations* defined by the alignment of mineral long axes; and (3) *modal layer contacts* defined by variations in mineral abundances (e.g., Higgins, 1991; Meurer and Boudreau, 1998). Here we predict the rock fabrics likely to result from the proposed layering hypotheses, for comparison with field and rock magnetic fabric data collected in this study.

The open system model suggests that black and red layers form through in situ crystallisation, and white layers form through a combination of gravitational settling and in situ crystallisation (Hunt et al., 2017). The closed system model suggests gravitational settling is the main layering mechanism for black, red and white layers. In situ nucleation and growth will typically produce no (i.e. isotropic) fabric (Meurer and Boudreau, 1998), whereas gravitational settling of crystals will produce a mineral foliation (e.g., Hess, 1960; Jackson, 1961; Meurer and Boudreau, 1998). Therefore, the open system model would likely produce no fabrics in the black and red layers, and potentially foliations within the white layers (**Fig. 3a**). In contrast, the closed system model would likely produce near-horizontal foliations across all layers (**Fig. 3b**) (Meurer and Boudreau, 1998). Critically, magmatic fabrics may be modified by processes such as: (1) magmatic flow over the crystal pile; (2) post-crystallisation compaction of the crystal pile; or (3) pre-consolidation shearing along inclined surfaces (e.g., Higgins, 1991; Meurer & Boudreau, 1998; Young & Donaldson, 1985). We therefore also explore the potential impacts of these processes.

Methodology

Sampling and logging

To record structural, textural, and modal mineral variations in the kakortokites we collected oriented core samples and stratigraphic logs during a 6-week expedition to Ilímaussaq in 2022. High spatial resolution sampling and logging were focused on two localities where Unit 0, which contains the clearest igneous layering in the field (Bohse et al., 1971), is well exposed. At Locality 1, Laksetværelv, sampling and logging were conducted across layers -1W, 0B, 0R, 0W and +1B (**Fig. 4**). At Locality 2, Kringlerne Cliff, Unit 0 was sampled and logged at a lower resolution relative to Locality 1 due to the nature of the outcrop, but more units were studied including layers -1W, 0B, 0R, 0W, +1B, +1R, +1W, +2B, +2R and +2W (**Fig. 4**). Where possible, core samples were collected perpendicular to the observed modal layering, and stratigraphic logging was conducted along the sampling transect. Sampling was conducted with a handheld drill with a 25 mm diameter non-magnetic diamond-tipped drill bit. Core orientations were measured using a Pomeroy orienting fixture. Sample locations were recorded using a GPS and on 1:100 scale window maps. At the University of St Andrews, standard 25 mm x 21 mm cylindrical sub-specimens were cut from the core samples using a non-magnetic diamond-edged circular saw.

<u>Rock magnetic analyses</u>

An essential part of all rock magnetic studies is determining the relationship between the magnetic fabric and the crystal fabric. Typically, magnetic long and short axes are parallel to crystal long and short axes, respectively, meaning we can use AMS to measure petrofabric orientations (e.g., Tarling and Hrouda, 1993). However, whilst AMS is a useful tool, it does provide a mean magnetic measurement of a sample, so combines the magnetic contributions of all diamagnetic, paramagnetic, and ferromagnetic minerals in a rock (e.g., Tarling and Hrouda, 1993; O'Driscoll et al., 2008; Bilardello, 2016). Therefore it may lead to complications if: (1) multiple fabrics are present within a sample (i.e., the AMS will only record one, possibly hybrid fabric); (2) the dominant magnetic minerals have an inverse AMS (e.g. single-domain magnetite), whereby the magnetic long and short axes are parallel to the crystal short and long axes, respectively (**Fig. 5a**) (Ferré, 2002; Černý et al., 2020); or (3) mineral properties such as chemistry, abundance, mineral alignment, and grain size, cause the AMS fabric to be oblique to the petrofabric (Biedermann et al., 2015b, 2015a, 2018; Bilardello, 2016; Biedermann, 2018). For example, cation substitutions in amphiboles result in contrasting unit cell structures with differing responses to external magnetic fields and AMS analysis (Biedermann et al., 2015a; Biedermann, 2018). It is therefore essential to characterise the mineral phases that dominate an AMS response and use other forms of textural analysis such as crystallographic preferred orientation (CPO) to interrogate AMS data (e.g., O'Driscoll et al., 2008, 2015). Measuring the ferromagnetic mineral fabric in isolation, to determine if the AMS is magnetically inverse or if there are multiple competing fabrics, is therefore highly beneficial and is achieved here using Anisotropy of Magnetic Remanence (AMR) (e.g., Jackson, 1991; Mattsson et al., 2021).

Anisotropy of magnetic susceptibility analyses

The AMS tensor, which can be represented by an ellipsoid, has three principal susceptibility axes: $K_1 \geq K_2 \geq K_3$ (**Fig. 5a**) (Tarling & Hrouda, 1993). The following parameters, based on the principal susceptibility axes and their corresponding natural logarithms (n_1, n_2, n_3) can be used to describe the AMS tensor:

$$\text{Mean susceptibility, } K_{mean} = (K_1 + K_2 + K_3)/3 \text{ (Tarling and Hrouda, 1993)} \quad (1)$$

$$\text{Degree of anisotropy, } P_j = [(n_1 - n)^2 + (n_2 - n)^2 + (n_3 - n)^2] \text{ (Jelinek, 1981)} \quad (2)$$

$$\text{Shape factor, } T = (2n_2 - n_1 - n_3)/(n_1 - n_3) \text{ (Jelinek, 1981)} \quad (3)$$

K_{mean} provides insight into the mineralogy of the sample, as minerals have different susceptibility values depending on whether they are diamagnetic, paramagnetic or ferromagnetic (Tarling and Hrouda, 1993). P_j describes the eccentricity of the AMS ellipsoid, i.e. the strength of the fabric, and T describes the shape (prolate or oblate) of the AMS ellipsoid (**Fig. 5b**).

Low-field AMS and bulk susceptibility measurements were acquired using an AGICO KLY-5A Kappabridge (400 Am^{-1} peak field, 1220 Hz peak frequency, room temperature) in the M^3Ore lab at the University of St Andrews. From Locality 1, 369 sub-specimens were analysed from 32 sample sites and 310 sub-specimens were analysed from 26 sample sites from Locality 2. Results are reported as mean AMS tensors averaged across a sample site, normalised by sample site mean susceptibility

(Jelinek, 1981). Variability across a sample site is shown with 95% confidence ellipses around principal axes, calculated by a tensor-averaging method by Jelinek (1981) (**Fig. 5a**). All raw data processing was completed in the software SAFYR7 and data was plotted and the site mean fabric was analysed in Anisoft 42.

Magnetic characterisation

As AMS is a bulk measurement of all minerals within a sample, temperature-susceptibility experiments were conducted to determine the mineral phase that dominates the magnetic susceptibility of the specimens. This is possible because diamagnetic, paramagnetic and ferromagnetic mineral susceptibilities behave differently with temperature (Dunlop and Özdemir, 1997). For diamagnetic minerals, susceptibility does not change with temperature whereas for paramagnetic minerals, susceptibility decreases with increasing temperature (Dunlop and Özdemir, 1997). The susceptibility of ferromagnetic minerals does not change with temperature until the Curie temperature (T_c) is reached, at which point the susceptibility decreases with temperature (Dunlop and Özdemir, 1997).

In this study, temperature-susceptibility experiments were conducted on samples from seven representative sites. Samples from a black, red and white layer from both Locality 1 and 2 were selected, including one duplicate red sample. Sub-specimen off-cuts were crushed using a ceramic pestle and mortar. A ~0.3 g split of rock pulp was analysed using an AGICO CS-L and CS4 attached to an AGICO KLY-5A Kappabridge. An inducing field of 400 Am^{-1} field at 1220 Hz was applied, and bulk magnetic susceptibility was measured every 25 seconds as a sample was (1) heated from -194˚C to room temperature, (2) heated from room temperature to 700˚C and cooled back down to room temperature, and then (3) heated from -194˚C to room temperature again, to produce a near complete heating cooling system between -194 ˚C and 700 ˚C. Raw data was processed using SAFYR 7, holder corrections and Curie Point estimates were calculated in Cureval 8.

In addition to temperature-susceptibility experiments, saturation isothermal remanent magnetisation (SIRM) and backfield isothermal remanent magnetisation (BIRM) were completed on nine representative sub-specimens to assess the coercivity of remanence-carrying particles in the samples (see Dunlop and Özdemir, 1997). Duplicate experiments were run on two sub-specimens to ensure consistency of the results. SIRM is achieved by imparting the sub-specimens with a stepwise increasing IRM pulse and measuring the remanent magnetisation of the sub-specimen between each magnetic pulse. Magnetic pulses are applied to the sub-specimen until it becomes magnetically saturated, at which point BIRM is measured by applying magnetic pulses in the opposite direction of the SIRM field. Magnetic pulses were applied with an MMPM 10 pulse magnetiser and remanent magnetisation was measured with an AGICO JR-6A spinner magnetometer.

Anisotropy of magnetic remanence analysis

To investigate the ferromagnetic fabric only, anisotropy of anhysteretic remanence (AARM) was completed on 25 representative sub-specimens from Locality 1 and 35 representative sub-specimens from Locality 2. AARM was completed using the 15-position rotational measurement scheme P-mode outlined by the AGICO REMA6 guidelines (Jelinek, 1977); an anhysteretic remanence magnetisation (ARM) was applied in 15 sample orientations, with demagnetisation steps occurring between each change in orientation. Samples were demagnetised and magnetised with an AGICO LDA5 and PAM1, and magnetic remanence was measured using a JR-6A spinner magnetometer. Demagnetisation steps were completed with a 200 mT alternating field (AF) in an automatic 2-axis tumbling specimen holder. ARM was imparted using a 100 µT direct current (DC) field, and a maximum AF of 200 mT.

<u>Petrography and crystallographic preferred orientation</u>

A total of 28 polished thin sections were created from representative sub-specimen AMS cores to examine mineral textures, mineral modal abundances, determine cumulus vs intercumulus phases, and assess the relationship between the petrographic and magnetic rock fabric data. Minerals with euhedral grain shapes or impingement textures were considered to be cumulus, whereas minerals with anhedral grain shapes defined by surrounding impinging minerals were considered to be intercumulus (Wager et al., 1960; Higgins, 2011). Thin sections were cut parallel to the AMS K_1 and K_3

susceptibility axes and perpendicular to modal layering to best capture the magnetic foliation and lineation (see **supplementary material**).

Four polished thin sections were made from sub-specimens to observe the general microstructure and perform crystallographic preferred orientation (CPO) analysis to compare the recorded magnetic fabrics with measured crystal fabrics. Samples 65 (black layer), 69 (red layer) and 77 (white layer) from Locality 1 were selected as representative samples from each layer of Unit 0, and sample 24 (black layer) from Locality 2 was selected as a representative sample from layer +2B. Crystallographic preferred orientations were obtained by electron backscatter diffraction analyses (EBSD) at the University of Leeds. A FEI Quanta 650 FEG-ESEM with Aztec software and an Oxford Symmetry EBSD detector were used to collect EBSD maps and EDS spectra covering roughly 1 cm^2 of the thin sections. EDS data was used to confirm phases identified by EBSD. Acquisition settings were 30 kV, 27 mm working distance, 70˚ specimen tilt and step sizes of 5 µm and 7 µm depending on grain size. Automatic indexing of arfvedsonite, alkali feldspar, nepheline and eudialyte was completed using the AZtec software (Oxford Instruments) and AZtecCrystal was used to complete standard noise reduction and produce pole figures. Pole figures are presented in the ZX plane (see **supplementary material**), lower hemisphere, 10˚ contour half width, and a contour range of 0–4 applied to all plots. Pole figures were reorientated to the geographic coordinate system for direct comparison with rock magnetic data (see **supplementary material**). The number of grains identified is in the range of 50–200. All point analyses are shown.

<u>Summary of fabric terminology</u>

Magnetic long/short axes: these axes refer to the long and short axes of the AMS ellipsoid.

Crystal long/short axes: these axes refer to the long and short shape axes of a crystal.

Crystallographic axes (a <100>, b <010>, c <001>): these axes refer to the crystallographic axes of a crystal and do not necessarily correspond in length with the crystal shape axes.

Silicate mineral fabric: a fabric (foliation and/or lineation) defined by the aligned shape of the silicate minerals within a rock.

Anisotropy of magnetic susceptibility fabric (AMS K_1, K_2, K_3): a magnetic fabric (foliation and/or lineation) defined by the combined contribution of diamagnetic (e.g. feldspar), paramagnetic (e.g. amphibole), and ferromagnetic (e.g. magnetite) minerals within a rock.

Anisotropy of anhysteretic remanent magnetisation fabric (AARM R_1, R_2, R_3): a magnetic fabric (foliation and/or lineation) defined solely by the ferromagnetic (e.g. magnetite) minerals within a rock.

Results

Field observations

We identify that the attitude of the modal layering is spatially variable and a mineral foliation, defined by alkali feldspar, is oblique to the modal layering (**Fig. 6b & d**). To the SE of a large naujaite outcrop, the modal layers have a bowl-like form dipping ~25˚ SE in the West, and ~15˚ NW in the East (**Fig. 6a**). Along the Kringlerne cliff the modal layers are roughly planar, dipping ~13˚ towards the North, and at Locality 1 the layers dip 39˚ towards the NE (**Fig 6b & d**). Unit +3 contains roof rock autoliths within its white layer, deflecting the modal layers both above and below (**Fig 6c**).

A mineral foliation defined by alkali feldspar is present across the kakortokites (**Fig. 6b, 7, 8c & 8d**); the alkali feldspar typically has a tabular habit with occasional kinking observed in black and white layers (**Fig. 8a & b**). Kinking of alkali feldspar mostly occurs where cumulus alkali feldspar grains are tightly packed, with grains abutting one another. The degree of alkali feldspar alignment varies through the layers appearing weakest in the centre of red layers, and strongest in black layers (**Fig. 7**). The degree of mineral alignment of alkali feldspar within white layers is variable (**Fig. 7**). The mineral foliation defined by alkali feldspar is often oblique in both strike and dip to modal layering, and crosscuts modal layer boundaries; this obliquity was observed in the NE of the kakortokites (**Fig. 6b & d**). The obliquity between the strike of the mineral foliation and modal layering ranges from ~10˚ to

~45˚; the strike of mineral foliations and modal layering are typically SW-NE or NW-SE (**Fig. 6b & d**). Modal layering typically dips more steeply than the mineral foliation, with the degree of obliquity ranging from sub-parallel to ~35˚ (**Fig. 6b & d**). At Locality 2 the mineral foliation is slightly steeper than the modal layering by ~10˚. One mineral lineation defined by arfvedsonite was observed in the field at Locality 2; the lineation (27˚→311) is near-parallel to the strike of the mineral foliation (341/19˚ NE), and trends in the dip direction of modal layering (220/13˚ NW) (**Fig. 6d & 8g**).

Geological log sections show that layers -1W, 0B, 0R, 0W, and +1B at Localities 1 and 2 have remarkably similar grain size variations and mineral textures (**Fig. 7**). The thickness of the layers varies between units, with white layers often three to five times thicker than black and red layers; the black and red layers typically vary from 0.5–2 m thick, and white layers typically range from 3–10 m thick (**Fig. 1c & 7**). Centimetre-scale layering within the kakortokites was also observed with more varied modal compositions and no consistency with regards to layer thickness (**Fig. 8l**). Layer -1W comprises densely packed, large (~1 cm) cumulus alkali feldspar laths with mainly intercumulus arfvedsonite (**Fig. 7 & 8b**). The transition from -1W to 0B is relatively sharp, occurring over 1 cm; at Locality 1 an aegirine vein ~1 cm wide follows the contact of the modal layering (**Fig. 6b & 7**). Besides the aegirine vein at Locality 1, aegirine is present in minor quantities through the layers, typically ~1% modal abundance; aenigmatite is also present in minor quantities <1% (**Fig. 7**). Layer 0B fines upwards and comprises mostly fine-grained cumulus arfvedsonite, between strongly aligned 0.5–1 cm cumulus alkali feldspar laths (**Fig. 7 & 8d**). Arfvedsonite within layer 0B often has irregular, patchy zoning, and sometimes has a granular texture (**Fig. 8k &** see **supplementary material**). The transition from 0B to 0R is gradual over 10 cm (**Fig 4a & 7**). Layer 0R coarsens upwards and has densely packed cumulus eudialyte and alkali feldspar with intercumulus arfvedsonite at its base, which becomes oikocrystic surrounding nepheline upwards through the layer (**Fig. 7**). Patchy alteration of alkali feldspar, nepheline and eudialyte is associated with white veining present within 0R at Locality 1 (**Fig. 7**). The transition from 0R to 0W gradually occurs over 20–30 cm (**Fig. 7**). The base of 0W is dominated by a finer-grained (<5 mm) intercumulus nepheline groundmass with larger (~1 cm) cumulus alkali feldspar laths (**Fig. 7, 8e**

& 8j). Arfvedsonite occurs as large (1–2 cm) oikocrysts containing nepheline; irregular, wavy grain boundaries are present around the nepheline indicative of disequilibrium between the nepheline and arfvedsonite (**Fig. 7, 8e & 8f**). Approximately halfway through layer 0W arfvedsonite is no longer oikocrystic, and becomes cumulus and intercumulus between densely packed cumulus alkali feldspar laths (**Fig. 7**). Layers +1B and +1R are poorly defined with a gradual transition between the two occurring over 10 cm; these layers contain coarse-grained cumulus arfvedsonite ~1 cm, with minor amounts of intercumulus arfvedsonite (**Fig. 7**). Layer +1W fines upwards and comprises densely packed cumulus alkali feldspar laths; arfvedsonite is mostly cumulus throughout the layer (**Fig. 7**). Layers +2B, +2R, and +2W are remarkably similar to +1B, +R, and +1W (**Fig. 7**). A common feature across all the layers is that intercumulus arfvedsonite often replaces areas of cumulus alkali feldspar (**Fig. 8b & i**).

Rock magnetic characterisation

Temperature-susceptibility results show a strong consistency across the samples, with Curie Temperatures (T_c), the temperature above which ferromagnetic minerals behave paramagnetically, ranging from 560˚C to 580˚C (**Fig. 9a & b**). A strong exponential decrease in susceptibility is observed between -194˚C and 400˚C, with another decrease in susceptibility occurring around 580˚C. These results indicate a large paramagnetic contribution, and minor contribution from magnetite, to the magnetic susceptibility at room temperature (Dunlop and Özdemir, 1997).

With the exception of sample 69, all black, red and white samples reach magnetic saturation ($M/M_0 > 0.95$) between 150 and 300 mT (**Fig. 9c**). Sample 69 reaches magnetic saturation at 1500 mT, significantly higher than the rest of the samples (**Fig. 9c**). BIRM curves show that all samples have relatively low remanence coercivity. With the exception of sample 69, white samples have the lowest coercivity, followed by red and then black samples (**Fig. 9d**). Samples that are easily magnetically saturated with low coercivity indicate the presence of magnetite (Dunlop and Özdemir, 1997). The higher magnetic saturation and coercivity of sample 69 are indicative of a different mineral phase being present, such as maghemite (Dunlop and Özdemir, 1997).

Magnetic susceptibility and anisotropy results

Magnetic parameters

K_{mean}, P_j and T display clear patterns that coincide with logged mineral and textural changes through the layered sequence (**Fig. 10**). K_{mean} values range from 2.09 x 10^{-3} to 2.67 x 10^{-4} (SI), with the highest K_{mean} values in the samples with the highest arfvedsonite content, and a steady decrease in K_{mean} as arfvedsonite content decreases (**Fig. 10**). Degree of Anisotropy (P_j) ranges from 1.038 to 1.006, with the strongest P_j values typically occurring in black layers and at layer transitions (**Fig. 10**). Shape Factor (T, **Fig. 4b**) values range from -0.89 to 0.43 with almost all samples plotting in the prolate field; black samples have the most prolate fabrics (**Fig. 10**). K_{rem}, the K_{mean} of the AARM data, values range from 7.16 x 10^{-5} to 5.35 x 10^{-4} (SI), with no clear pattern observed between K_{rem} and mineral modal abundances.

Anisotropy of magnetic susceptibility (AMS) and anisotropy of anhysteretic remanence (AARM)

AMS data across both outcrops consistently display a sub-vertical K_1 with a sub-horizontal K_2 and K_3; all three susceptibility axes have well-constrained 95% confidence ellipses across all sample sites indicating that both a magnetic foliation and lineation are present (**Fig. 11**). While K_1 remains consistently sub-vertical across the dataset, the orientation of K_2 and K_3 rotates anticlockwise from SE towards the NE as the mineral mode varies across the layers (**Fig. 11 Stereonet A**). Samples that contain more arfvedsonite (i.e. black layers) have a K_3 that plots towards the NE, and as arfvedsonite content decreases (i.e. red and white layers), K_3 tends to plot towards the SE (**Fig. 11 Stereonet A**). At Locality 2 the plane to K_1 is near-parallel to the field-measured modal layering, except for sample 17 from layer +1B (**Fig. 11**). At Locality 1 the plane to K_1 is consistently oblique to the modal layering, with the plane to K_1 plane recording a near-horizontal dip whereas modal layering dips 39˚.

The AARM data displays two main trends: samples which have a NE-SW striking ferromagnetic foliation plane, and samples which have an NW-SE striking ferromagnetic foliation plane (**Fig. 11**). The samples that have NE-SW striking AARM foliations are from red and white layers (samples 06, 23, 29, 69, 77), whereas those that have NW-SE striking AARM foliations are from black layers and white layers containing oikocrystic arfvedsonite (samples 12, 17, 24, 27, 50, 75, 85; **Fig. 11**). All AARM foliations are highly oblique to orthogonal to the modal layering (**Fig. 11**). The AARM strike is nearly perpendicular to the modal layering in most samples and the difference in dip between the AARM foliation and the modal layering ranges from near parallel to ~90˚ (**Fig. 11**). The AARM data also shows a consistent magnetic lineation (R_1) that is well-defined and typically lies along the igneous layering plane (**Fig. 11**). The orientation of the AARM R_1 maintains a coaxial relationship with the orientation of the AMS K_2; this correlation is strongest in white layers and weakest in black layers (**Fig. 11**). In brief, the AARM suggests there is a ferromagnetic foliation that is orthogonal to modal layering with a consistent lineation along the modal layering plane.

<u>Crystallographic preferred orientation (CPO)</u>

CPO was completed on samples 65 (60% modal arfvedsonite), 69 (20% modal arfvedsonite) and 77 (10% modal arfvedsonite) from the black, red and white layers of Unit 0 at Locality 1, and on sample 24 (65% modal arfvedsonite) from layer +2B at Locality 2 (**Fig. 4b & 7**). Arfvedsonite exhibits varying degrees of mineral alignment as observed in CPO pole figures across the samples; a marked decrease in CPO is recorded in sample 77 with 10% modal arfvedsonite (**Fig. 12**). In sample 65 (layer 0B), the arfvedsonite shows a CPO with the (110) poles girdling a sub-horizontal plane, and the (001) poles normal to the sub-horizontal plane (**Fig. 12**). Sample 69 (layer 0R) shows a similar CPO to 65; a weak alignment of the (010) poles is also apparent in the NW quadrant of the stereonet (**Fig. 12**). In sample 24 (layer +2B) the arfvedsonite (010) poles are normal to the sub-horizontal plane with (001) poles girdling the sub-horizontal plane; this CPO is orthogonal to the arfvedsonite CPO in sample 65 (layer 0B) (**Fig. 12**). No clear CPO is observed in sample 77 (layer 0W). Alkali feldspar records a high degree of CPO across all samples; (100) and (001) poles girdle a sub-horizontal plane, and (010) poles are normal to the sub-horizontal plane (**Fig 12**).

Eudialyte records a clear CPO in samples 69 and 77 (**Fig. 12**). In sample 69 (0001) poles cluster in the NE quadrant, with (10-10) and (11-20) poles girdling a NW-SE plane dipping ~40˚ SW (**Fig 12**). Sample 77 records a eudialyte CPO orthogonal to sample 69; (0001) poles cluster in the SW quadrant, with (10-10) and (11-20) poles girdling a NW-SE plane dipping ~40˚ NE (**Fig 12**). No clear eudialyte CPO is recorded in samples 65 or 24 (**Fig. 12**). Nepheline records a high degree of CPO in samples from Unit 0; in samples 69 and 77 (0001) poles cluster in the SW quadrant and (10-10) poles girdle a NW-SE plane dipping ~40˚ SE (**Fig 12**). In sample 65 nepheline CPO is orthogonal to the other samples with (0001) poles clustering in the NE quadrant and (10-10) poles girdling a NW-SE plane dipping ~˚40 SW. A weak eudialyte CPO is recorded in sample 24 where (10-10) poles girdle a sub-horizontal plane, and (0001) poles are normal to the sub-horizontal plane (**Fig. 12**). It is noted that both eudialyte and nepheline have near-isotropic crystal morphologies and therefore while the CPO is consistent, the shape preferred orientation (SPO) of the minerals may not be.

<u>Field-observed modal layering, CPO, and magnetic fabric comparison</u>

In Unit 0 the sub-horizontal girdling of arfvedsonite (110) poles, and alkali feldspar (100) and (001) poles, are typically shallower than igneous layering by ~20˚ (**Fig. 12**). The girdling of eudialyte (10-10) and (11-20) poles, and nepheline (10-10) poles are typically parallel to igneous layering (**Fig. 12**). In layer +2B the sub-horizontal girdling of arfvedsonite (001) poles, alkali feldspar (100) and (001) poles, and (10-10) poles are all near parallel to igneous layering (**Fig. 12**). All minerals record a weak correlation between the grouping of the poles to crystal planes, and the orientation of the AARM axes (**Fig. 12**). Across all mineral phases, AARM axes correspond to varying poles to crystal planes (i.e. there is no consistent relationship between specific AARM axes and poles to crystal planes).

Arfvedsonite CPO in samples 65 and 69 correspond well to AMS axes; there is a grouping of (001) poles with AMS K_1, and (110) poles with AMS K_3 (**Fig. 12**). Sample 69 also records a grouping between arfvedsonite (010) poles and AMS K_2 (**Fig. 12**). Arfvedsonite CPO in sample 24 also corresponds well to AMS axes with (010) poles grouping with AMS K_1, and (001) poles grouping with AMS K_2 (**Fig. 12**). Across all samples, alkali feldspar CPO corresponds to AMS axes: (010) poles are coaxial with AMS K_1, (100) poles are coaxial with AMS K_2, and (001) poles are coaxial with AMS K_3. Eudialyte and nepheline CPO do not show a clear relationship with AMS axes (**Fig. 12**).

Discussion

Relationship between petrofabrics and magnetic fabrics

To identify the minerals that contribute to and dominate the magnetic fabrics recorded through the layers of the kakortokites at Ilímaussaq, we first identify the magnetic mineralogy of the rocks, and then relate the measured magnetic fabrics with silicate mineral fabrics identified in the field and through CPO analysis. By doing this we create a robust textural context of the layers allowing for the interrogation of previously proposed open and closed system layering hypotheses, which cite differing physical magmatic processes that should be recorded in the rock record (**Fig. 3**).

Magnetic mineralogy

The kakortokites largely comprise (25–75%) diamagnetic minerals, such as alkali feldspar and nepheline. Diamagnetic mineral phases have weak magnetic susceptibilities (typically ~1×10^{-6} SI) so are expected to have a negligible magnetic contribution to the kakortokites (e.g. Biedermann et al., 2016; O'Driscoll et al., 2008; Rosenblum & Brownfield, 2000; Tarling & Hrouda, 1993). Eudialyte has an isotropic morphology across all the samples and therefore is also unlikely to significantly contribute to the magnetic fabrics (O'Driscoll et al., 2024). In contrast, paramagnetic minerals, such as amphibole and pyroxene, typically have bulk magnetic susceptibility values of ~1×10^{-4} SI (Borradaile et al., 1987). Given that the K_{mean} values of our samples are >2.4×10^{-4} SI, and the strong exponential decrease in susceptibility from -190˚C to 400˚C observed in temperature-susceptibility experiments at both study sites (**Fig. 9a & b**), paramagnetic minerals likely make a substantial/dominant contribution to the bulk magnetic susceptibility. In our samples, the paramagnetic phases arfvedsonite, aegirine, and aenigmatite are all present (**Fig 7**) (Rosenblum and Brownfield, 2000). Aenigmatite occurs in ~1% modal abundance so likely does not contribute significantly to the bulk magnetic susceptibility. Aegirine occurs in ~1% modal abundance across most layers, with its highest abundance reaching ~5–10% in layer 0W at Locality 2. O'Driscoll et al. (2024) found that at Ilímaussaq aegirine has a much lower theoretical bulk susceptibility than arfvedsonite; given this and its low modal abundance, aegirine likely does not contribute significantly to the bulk susceptibility. Arfvedsonite occurs in 10–60% modal abundance and therefore is determined to be the dominant carrier of magnetic susceptibility. A clear relationship between bulk magnetic susceptibility and arfvedsonite abundance is observed at both Locality 1 and 2, where arfvedsonite-rich (>55%) black layers have the highest K_{mean} values (9.26×10^{-4} to 2.09×10^{-3} SI), and arfvedsonite-poor (<30%) white layers have the lowest K_{mean} values (2.37×10^{-4} to 9.50×10^{-4} SI) (**Fig. 10**); these observations further substantiate the interpretation that arfvedsonite dominates the bulk magnetic susceptibility.

In addition to the paramagnetic component, our rock magnetic analyses show that all samples contain a mineral phase that carries remanence, a feature unique to ferromagnetic and antiferromagnetic minerals (**Fig. 9c, 9d & 11**) (e.g., Tarling and Hrouda, 1993). All samples, except sample 69, reach 95% magnetic saturation in IRM fields below 200 mT and exhibit a ~560–580˚C Curie temperature (T_C) (**Fig. 9a-c**); these characteristics are consistent with the presence of magnetite (Dunlop and Özdemir, 1997). We do not observe any magnetite in our thin sections or on an SEM but note magnetite can be <1 µm, and occurs in very low abundance in these samples, making it undetectable using these methods (Dunlop and Özdemir, 1997). Sample 69 from layer 0R has a deep red discolouration and requires IRM fields above 1.5 T to reach 95% saturation, which could indicate the presence of maghemite (**Fig. 9c**) (Dunlop and Özdemir, 1997). Maghemite is known to form due to the partial oxidation of magnetite during hydrothermal alteration (Dunlop and Özdemir, 1997). Late-stage alteration associated with white veins cross-cutting the kakortokites was observed in the field at layer 0R (**Fig. 7**) supporting the interpretation that maghemite is a product of late-stage hydrothermal alteration. We do not observe any maghemite in our thin sections or on an SEM, however samples with minimal alteration were selected for thin section, which may explain why we do not observe it.

In summary, the main magnetic minerals within the kakortokites are arfvedsonite and magnetite. The bulk magnetic susceptibility is dominated by the paramagnetic contribution from arfvedsonite, with a minor ferromagnetic contribution from magnetite.

Carriers of anisotropy of magnetic susceptibility

If a rock contains ferromagnetic minerals and >10% paramagnetic minerals, as is the case for the kakortokites (**Fig. 7**), both the paramagnetic and ferromagnetic minerals will contribute to the AMS fabric (i.e. orientation of the magnetic fabric) (Tarling and Hrouda, 1993). Although arfvedsonite (10–60% modal abundance) is more abundant than magnetite (likely <<1% modal abundance) within our samples, previous studies have shown that magnetite may dominate AMS fabrics even if present in trace quantities (e.g., Borradaile, 1987, 1988; Clark, 1997; Parés, 2015; Biedermann et al., 2015a; Ageeva et al., 2017, 2020). Therefore, to interpret the magnetic fabric, we must first determine whether arfvedsonite or magnetite dominates the AMS.

CPO data provides valuable insight into the relationship between the silicate petrofabric defined by arfvedsonite and the magnetic fabrics. The correlation between AMS axes and CPO poles to arfvedsonite crystal planes weakens as arfvedsonite content decreases (i.e. compare arfvedsonite CPO from sample 65 with 77, **Fig. 12**). In contrast, the AARM axes, which only represent the ferromagnetic component of the samples, maintain a correlation with the poles to the crystal planes in all samples (**Fig. 12**). The grouping of the AARM data with the CPO poles of all minerals suggests that magnetite could be present as small (<1 μm) exsolved minerals within the silicate phases, or interstitially in orientations controlled by the silicate minerals. Therefore, while the paramagnetic component is recording the sub-horizontal foliation of arfvedsonite (**Fig. 12**), the ferromagnetic component defined by magnetite is recording a foliation normal to igneous layering. These two conflicting mineral fabrics, defined by arfvedsonite and magnetite, will both contribute to the AMS (Tarling and Hrouda, 1993).

Systematic variations in the contribution of the paramagnetic and ferromagnetic components to AMS correlate with changes in mineral abundance within the samples (**Fig. 11 Stereonet A**). Specifically, samples with higher magnetic susceptibility values ~1 x 10^{-3} SI (black layers) typically have AMS K_3, i.e. the pole to the magnetic foliation, plunging ~10˚ to the NE, whereas samples with lower magnetic susceptibility values ~1 x 10^{-4} (white layers) typically have AMS K_3 plunging ~10˚ to the SE (**Fig. 11 Stereonet A**). This NE-SE rotation of the AMS fabric is not recorded in the silicate fabric in the field or CPO data, suggesting that the rotation could be due to competing paramagnetic and ferromagnetic fabrics. For example, AARM R_1 and AMS K_2 have a weak correlation in black layers, and a stronger correlation in white layers (**Fig. 11**); we suggest this is evidence of the ferromagnetic contribution influencing the orientation of the AMS axes, causing the rotation of K_3 towards the SE when arfvedsonite abundance is low. Alternatively, the rotation of the AMS fabric may be due to changes in arfvedsonite chemistry. Lindhuber et al. (2015) recorded significant variability in arfvedsonite chemistry in white layers compared to black layers. This variation in mineral chemistry through the stratigraphic section could affect the AMS fabric (Biedermann et al., 2015a).

In summary, arfvedsonite dominates the AMS when it is present in high modal abundance in the black kakortokite layers, and magnetite may contribute a proportionally larger amount to the AMS in white layers with low arfvedsonite modal abundance. This interpretation is consistent with other layered intrusion studies that also find AMS varies in response to contributions by competing mineral fabrics (Maes et al., 2008; Ferré et al., 2009, 2012; Biedermann et al., 2016). The magnetite contribution is likely small, and the variations observed in the AMS fabric orientation may also be explained by changes in arfvedsonite chemistry. Given the variability in the orientation of the AMS fabric, care should be taken when interpreting the fabrics, particularly the magnetic lineation orientation.

Magnetic and silicate mineral fabric data in the context of field relationships

Both AARM and AMS data maintain a consistent relationship relative to the macroscopic silicate fabrics (**Fig. 12**). The AARM ferromagnetic fabric is highly oblique to orthogonal to the modal layering, recording a sub-vertical foliation defined by magnetite (**Fig. 11**). In our AMS data, K_1 is consistently orthogonal to the silicate mineral foliation of arfvedsonite and alkali feldspar (**Fig. 12**); i.e., the AMS fabric is therefore inverse to the silicate mineral fabric, such that the AMS K_1 records the pole to the mineral foliation, while either the AMS K_2 or K_3 records the mineral lineation (see Ferré, 2002). Similar inverse fabrics have been identified in previous studies in minerals such as single-domain magnetite, hematite, tourmaline, and amphibole (Borradaile and Henry, 1997; Borradaile and Gauthier, 2001; Ferré, 2002; Biedermann et al., 2015a, 2018; O'Driscoll et al., 2024). We note that while our AMS K_1 is consistently orthogonal to the silicate mineral foliation, the AMS K_1 is coaxial with arfvedsonite (001) poles in layer 0B, and coaxial with arfvedsonite (010) poles in layer +2B (**Fig. 12**). This relationship is in line with previous work completed on amphibole-bearing rocks where samples with differing CPO (e.g., girdle vs point distribution of crystallographic axes) produce similar AMS orientations (Biedermann et al., 2018). Given our inverse AMS results, sub-vertical AMS K_1 axes are attributed to the occurrence of a consistent sub-horizontal mineral foliation through all the igneous layers (**Fig. 11**). The sub-horizontal mineral foliation is near-parallel to modal layering at Locality 2, but oblique to modal layering at Locality 1 and the surrounding area (**Fig. 6b, 6d & 11**).

Well-constrained 95% confidence ellipses around AMS K_2 and K_3 suggest a mineral lineation is also present throughout the layers, although we cannot definitively determine which of K_2 or K_3 record the crystal long axes (**Fig. 11**). The presence of mineral lineations is supported by the observation of an arfvedsonite lineation in the field at Locality 2 (**Fig. 6d & 8g**). At Locality 1, the AMS K_2 and K_3 are oblique to layering, however at Locality 2, the AMS K_2 or K_3 coincide with the dip azimuth or the strike of modal layering; this suggests at Locality 2 there is a mineral lineation oriented within the modal layering whereas at Locality 1 there is a mineral lineation oblique to the modal layering (**Fig. 11**).

Testing layering models using magnetic and crystal fabric data

To interpret our fabric data within the kakortokites, we must first establish whether the fabrics are primary magmatic or a tectonic overprint. Regional sinistral transcurrent faulting was potentially active during and after the emplacement of the Ilímaussaq complex (Chadwick and Garde, 1996; Upton, 2013b). Post-magmatic overprinting would likely result in the re-alignment of earlier fabrics with the wider tectonic stress field or local deformation zones (Benn et al., 1998; Žák et al., 2005; McCarthy et al., 2015; Burton-Johnson et al., 2019; Latimer et al., 2024). The orientation of the mineral foliations and lineations are highly oblique to previously proposed strike slip faulting, and zones of concentrated sub-vertical shearing are not observed in the outcrops visited (**Fig. 7**). Evidence of brittle deformation is not identified within the kakortokites, however occasional kinking of alkali feldspar suggests some dynamic recrystallisation occurred (**Fig. 7 & 8b**) (e.g., Ferré et al., 2002; Knight & Walker, 1988; Maes et al., 2007). Therefore, the fabrics observed in the kakortokites are considered to be magmatic in origin rather than a post-magmatic tectonic overprint. Thus, the fabrics within the kakortokites represent magmatic state and crystal mush processes only.

Having established the fabrics we record are likely magmatic, we now examine how they compare to previous layering hypotheses. The open system model invokes in situ crystallisation for black and red layers, and gravitational settling within white layers (Hunt et al., 2017). The change from in situ crystallisation to gravitational settling should result in white layers having the strongest mineral foliations, whereas black and red layers should have the weakest or no fabrics (**Fig. 2a & 3**) (Meurer and Boudreau, 1998); this is inconsistent with our data, which shows the strongest mineral alignment is within black layers (**Fig. 7 & 10**). Additionally, in the open system model, compaction of the crystal pile is used to explain all foliations in the layers across kilometres of the intrusion (Hunt et al., 2017). While compaction may cause reorientation of crystals within a mush, it is debated how effective compaction is at forming consistent, well-defined foliations, making it a questionable sole source of the foliations observed in the kakortokites (Higgins, 1991; Meurer and Boudreau, 1998; Holness et al., 2017; Bachmann and Huber, 2019; Kruger and Latypov, 2022). The oblique relationship observed in our data between the mineral foliation and the modal layering (**Fig. 6b**) is also difficult to reconcile with an open system model (**Fig. 2a**). If a primitive magma were to be injected over the crystal pile to form a new black layer, it would likely erode, disrupt, and/or form a new fabric at the layer boundary; this is inconsistent with our observations showing the foliation defined by alkali feldspar crosscuts the -1W/0B modal layering boundary, maintaining continuity irrespective of the layer change (**Fig. 6b**). Therefore, we suggest that the CSD data in Hunt et al. (2017) that is indicative of in situ nucleation and crystal growth, largely reflects post-accumulation textural coarsening of the crystal pile. This is supported by significant overgrowths making up 10–50% of eudialyte as recorded by Borst et al. (2018), and the partially granular texture of layer 0B observed in thin section, which has curvilinear grain boundaries and 120˚ three-grain junctions (**Fig. 8i, k &** see **supplementary material**).

In the closed system model, gravitational settling of crystals would be expected to produce foliations across entire igneous layers (**Fig. 2b & 3b**); this is consistent with our data, which records continuous sub-horizontal mineral foliations through the layers (**Fig. 11**) (Meurer and Boudreau, 1998). The closed system model also suggests arfvedsonite and alkali feldspar mats form simultaneously, with alkali feldspar mats becoming trapped beneath arfvedsonite mats (Bons et al., 2015; Lindhuber et al., 2015). The contemporaneous formation of adjacent black and white layers is supported by our observation of a continuous alkali feldspar foliation across layer boundaries (**Fig. 6b**). The quasi-closed mush compartments proposed in the closed system model may also be supported by the difference in arfvedsonite shape and CPO between the layers in Unit 0 and layer +2B (**Fig. 12**). In layer +2B we observe elongate arfvedsonite crystals that define a sub-horizontal foliation (**Fig. 8g & h**), however in layer 0B arfvedsonite crystals are observed as a stubby groundmass (**Fig. 8a, d, i, &** see **supplementary material**). The difference in arfvedsonite crystal shape between layers +2B and 0B coincides with a change in arfvedsonite CPO (**Fig. 12**). In layer +2B the arfvedsonite (010) poles are sub-vertical and normal to the silicate foliation, whereas in layer 0B the arfvedsonite (001) poles are sub-vertical and normal to the silicate foliation (**Fig. 12**). As arfvedsonite is typically elongate along [001] (Gordon, 1927; Hogarth et al., 1987), we would generally expect sub-horizontal (001) poles and sub-vertical (010) poles normal to the silicate foliation, as is recorded in layer +2B (**Fig. 12**). We suggest that arfvedsonite crystal habit may vary between layered units, and perhaps has a stubby habit in layer 0B, compared to a more elongate habit in layer +2B (see idealized crystal shapes, **Fig. 12**). While few studies have investigated changes in amphibole habit, work on feldspars has shown that their habit varies between prismatic and tabular with changes in cooling rate (Holness, 2014) or the degree of undercooling (Mangler et al., 2022). Recent amphibole crystallisation experiments from crushed basalt samples revealed crystal shape and size differences with changes in temperature, pressure, and crystallisation time (Zhang et al., 2019). Amphibole shape varies from bladed to prismatic with increasing temperature or time, and from bladed to tabular with increasing pressure, suggesting that like feldspar, amphibole habits are sensitive to magmatic conditions (Zhang et al., 2019). If arfvedsonite crystals have a stubby morphology, gravitational settling of the crystals would form sub-horizontal foliations along the (001) crystal faces as recorded in layer 0B (**Fig. 12**). In contrast, gravitational settling of acicular arfvedsonite elongate along [001] would form foliations along the (010) crystal faces, as recorded in layer +2B (**Fig. 12**). Vertical (001) poles in layer 0B may also explained by in-situ growth with a vertical chemical or temperature gradient in a process similar to how dendrites or comb layering form (e.g., Lofgren and Donaldson, 1975; O'Driscoll et al., 2007), however this would imply significant heterogenous nucleation (arfvedsonite nucleating on other arfvedsonite) within layer 0B occurred, which is an energetically unfavourable process (Wieser et al., 2019; Holness et al., 2023). Overall, we suggest changes in arfvedsonite CPO across layered units likely records variations in arfvedsonite habit due to differences in magmatic conditions, and subsequent gravitational settling. This would suggest there were slight variations in temperature, pressure and/or chemistry between layered units, supporting that continued gravitational settling within quasi-closed mush compartments occurred (Borst et al., 2018).

Although the closed system model explains the recorded mineral foliations within the kakortokites, it does not explain the presence of a lineation through the layers, or how the oblique relationship between the mineral foliation and the modal layering formed. Kinked alkali feldspar (**Fig. 8b**) and the obliquity between the mineral foliation and modal layering (**Fig. 6b & d**) indicate that a post-cumulus modification process, likely occurred (Meurer and Boudreau, 1998; Selkin et al., 2014). We suggest that two stages of post-cumulus compaction via crystal repacking offers an explanation for the lineations and oblique relationships recorded in this study (**Fig. 13**). To explain the obliquity between the mineral fabric and modal layering, the area where the obliquity is recorded must be considered. Obliquity is observed in the region at and around Locality 1 (**Fig. 13a**). Notably, this region contains a variety of roof rock autoliths, whereas no large autoliths are recorded immediately around Locality 2, where the mineral fabric and modal layering are parallel (**Fig. 13a**). In regions with no autoliths, gravitational settling of crystal mats would likely form a sub-horizontal mineral foliation that is parallel to modal layering (**Fig. 13ci & 13cii**). Any subsequent pure compaction of these mats would then enhance pre-existing sub-horizontal foliations. If the gravitational settling and compaction process occurs where the floor of the magma reservoir is inclined, compaction should have an element of shear to it, producing mineral lineations (**Fig. 13civ**). We suggest this is the process we record at Locality 2, where the modal layering and mineral foliation are near-parallel and sub-horizontal, and arfvedsonite lineations are present (**Fig. 8g, 11 & 13civ**). In contrast, areas where autoliths sink onto the crystal pile may instigate differential compaction of the layers immediately below them (**Fig. 13cii**). Differential compaction due to sinking autoliths may deform previously sub-horizontal layers, causing them to deflect around the shape of the autolith (**Fig. 13cii**), as was observed in the field (**Fig. 6c**). At this stage the mineral foliation may remain parallel to the modal layering (**Fig. 13cii**). However, as layers continue to develop, compaction through crystal repacking across the entire crystal pile may occur if interstitial melt migrates up through the crystal pile (**Fig. 13civ**). Critically, intrusion-wide compaction of the crystal pile may not cause large-scale mineral redistribution, leaving the modal layering attitude unaffected (**Fig. 13civ**). However, intrusion-wide compaction could flatten pre-existing mineral foliations (**Fig. 13civ**), particularly foliations defined by elongate minerals (i.e. arfvedsonite and alkali feldspar), through crystal repacking, causing obliquity between the mineral foliation and modal layering (**Fig. 6b, 11, 12 & 13civ**) (Holness et al., 2017; Holness, 2018; Bachmann and Huber, 2019). Smaller, isotropic minerals (i.e. nepheline and eudialyte) likely would not rotate significantly during crystal repacking due to their near-spherical morphology (Bachmann and Huber, 2019), explaining why they remain parallel to modal layering as recorded in our CPO data (**Fig. 12**). We suggest the vertical migration of melt during compaction is recorded by our sub-vertical magnetite fabric (**Fig. 11**), as well as the disequilibrium textures observed in arfvedsonite oikocrysts (**Fig. 7 & 8f**).

A closed system model with compaction

In our closed system model, crystal mats form through hindered settling (**Fig. 2b**) towards the bottom of the magma reservoir (**Fig. 13ci**). The crystal mats continue to develop from the bottom of the magma reservoir up, supported by the upwards fractionation trends through the kakortokites recorded by Borst et al. (2018) (**Fig. 13ci**). Continued crystal growth causes the crystal mats to form semi-impermeable mush compartments, isolating melt within them that continues to evolve (**Fig. 13ci**) (Bons et al., 2015; Lindhuber et al., 2015; Borst et al., 2018). During the development of the crystal mats, large roof autoliths sink onto the crystal pile (**Fig. 13cii**). The autoliths locally cause differential compaction of the layers below them, and crystal mats that form after the deposition of the autoliths drape above them (**Fig. 13cii & 13ciii**). As the crystal mats continue to develop, vertical migration of interstitial melt allows for compaction via crystal repacking to occur across the intrusion (**Fig. 13civ**). The continued compaction of the crystal pile does not affect the modal layering attitude, but causes the foliation of elongate minerals, such as arfvedsonite and feldspar, to flatten (**Fig. 13civ**), creating the obliquity between the mineral foliation and modal layering, as recorded in field, AMS, and CPO data (**Fig. 6b, 6d, 11 & 12**).

Our data support a closed magmatic system model where igneous layers form through the accumulation of crystal mats. A similar process was invoked to explain the formation of plagioclase and pyroxene macrolayers within the mafic Skaergaard intrusion (Nielsen et al., 2015), suggesting that the magmatic processes recorded in this study are not unique to alkaline intrusions, and may be applicable to layered intrusions of varying compositions. Our data also support the interpretation that significant REE deposits are formed from a single major melt injection, which subsequently mechanically self-sorts through gravitational settling to create REE-enriched horizons. Our findings support a growing consensus that petrofabric analyses are powerful tools in deciphering mechanisms of igneous layering.

Conclusions

Combining field structural relationships, petrography, crystallographic preferred orientations, and magnetic fabric data has allowed for the interrogation of hypothesised igneous layering mechanisms. Due to large variations in the modal composition of the igneous layers, combining anisotropy of magnetic susceptibility with anisotropy of anhysteretic remanence, crystallographic preferred orientations, and high spatial resolution stratigraphic logging is essential for gaining a comprehensive perspective on the rock fabric. Our magnetic data show that arfvedsonite and magnetite both contribute to the AMS; their relative contributions vary through the layered stratigraphy. Comparison of the AMS fabric with fabrics recorded in the field and CPO show that our magnetic fabric is inverse to the silicate fabric defined by arfvedsonite and alkali feldspar. Our data record a consistent sub-horizontal silicate mineral foliation and lineation. Critically, the silicate fabric can be oblique to modal layering in both strike and dip. The consistent presence of both a mineral foliation and lineation through the modal layers, and the obliquity between the silicate fabric and modal layering, calls into question previous studies which have cited in situ nucleation and growth as the main mechanism in igneous layering. Our data best supports a closed magmatic system model, where igneous layers form through crystal mat accumulation. Obliquity between the silicate fabric and modal layering suggests that the crystal pile was likely impacted by differential compaction due to roof rock collapse and subsequent intrusion-wide compaction.

Acknowledgements

Field context and samples were collected for this study during a field expedition to Ilímaussaq in 2022. The expedition was funded by the Geological Society of London, Gino Watkins Memorial Fund, the Arctic Club, the Society of Economic Geologists, the Cambridge Arctic Shelf Programme, the Henry Emeleus award of the Volcanic and Magmatic Studies Group, the Hazel-Prichard Student Bursary, and the Edinburgh Geological Society. We thank Tesni Morgan, Aithne Lawrence, Nina Brendling, Yasamin Bayley, and Brogan Smith for their support during the field expedition. We also thank A. Borst and an anonymous reviewer for detailed and constructive reviews, and K. Yoshida for editorial handling.

Funding

This work was supported by the Natural Environment Research Council via an IAPETUS2 PhD studentship held by Emily Jones (grant reference NE/S007431/1). William Hutchison is funded by a UKRI Future Leaders Fellowship (MR/S033505/1).

Data Availability

The datasets generated and/or analysed during the current study are available in the Mendeley Data repository, http://doi.org/10.17632/7xcf2cpr7g.2

References

Ageeva, O., Bian, G., Habler, G., Pertsev, A., and Abart, R., 2020, Crystallographic and shape orientations of magnetite micro-inclusions in plagioclase: Contributions to Mineralogy and Petrology, v. 175, doi:10.1007/s00410-020-01735-8.

Ageeva, O., Habler, G., Pertsev, A., and Abart, R., 2017, Fe-Ti oxide micro-inclusions in clinopyroxene of oceanic gabbro: Phase content, orientation relations and petrogenetic implication: Lithos, v. 290–291, p. 104–115, doi:10.1016/j.lithos.2017.08.007.

Andersen, S., Bohse, H., and Steenfeld, A., 1988, The Southern Part of the Ilimaussaq Complex, South Greenland, 1:20,000: Grønlands Geologiske Undersøgelse,.

Andersen, S., Bohse, H., and Steenfelt, A., 1981, A geological section through the southern part of the Ilímaussaq intrusion: Rapport Grønlands Geologiske Undersøgelse, v. 103, p. 39–42, doi:10.34194/rapggu.v103.7729.

Bachmann, O., and Huber, C., 2019, The Inner Workings of Crustal Distillation Columns; The Physical Mechanisms and Rates Controlling Phase Separation in Silicic Magma Reservoirs: Journal of Petrology, v. 60, p. 3–18, doi:10.1093/petrology/egy103.

Bailey, J.C., Gwozdz, R., Rose-Hansen, J., and Sørensen, H., 2001, Geochemical overview of the Ilímaussaq alkaline complex, South Greenland: Geology of Greenland Survey Bulletin, v. 190, p. 35–53, doi:10.34194/ggub.v190.5172.

Benn, K., Ham, N.M., Pignotta, G.S., and Bleeker, W., 1998, Emplacement and deformation of granites during transpression: magnetic fabrics of the Archean Sparrow pluton, Slave Province, Canada: Journal of Structural Geology, v. 20, p. 1247–1259, doi:10.1016/S0191-8141(98)00065-0.

Biedermann, A.R., 2018, Magnetic anisotropy in single crystals: A review: Geosciences, v. 8, p. 1–16, doi:10.3390/geosciences8080302.

Biedermann, A.R., Heidelbach, F., Jackson, M., Bilardello, D., and McEnroe, S.A., 2016, Magnetic fabrics in the Bjerkreim Sokndal Layered Intrusion, Rogaland, southern Norway: Mineral sources and geological significance: Tectonophysics, v. 688, p. 101–118, doi:10.1016/j.tecto.2016.09.019.

Biedermann, A.R., Koch, C.B., Pettke, T., and Hirt, A.M., 2015a, Magnetic anisotropy in natural amphibole crystals: American Mineralogist, v. 100, p. 1940–1951, doi:10.2138/am-2015-5173.

Biedermann, A.R., Kunze, K., and Hirt, A.M., 2018, Interpreting magnetic fabrics in amphibole-bearing rocks: Tectonophysics, v. 722, p. 566–576, doi:10.1016/j.tecto.2017.11.033.

Biedermann, A.R., Pettke, T., Bender Koch, C., and Hirt, A.M., 2015b, Magnetic anisotropy in clinopyroxene and orthopyroxene single crystals: Journal of Geophysical Research: Solid Earth, v. 120, p. 1431–1451, doi:10.1002/2014JB011678.

Bilardello, D., 2016, Magnetic Anisotropy: Theory, Instrumentation, and Techniques, *in* Reference Module in Earth Systems and Environmental Sciences, Elsevier, doi:10.1016/b978-0-12-409548-9.09516-6.

Bohse, H., Brooks, C.K., and Kunzendorf, H., 1971, Field observations on the kakortokites of the Ilímaussaq intrusion, South Greenland, including mapping and analyses by portable X-ray fluorescence equipment for zirconium and niobium: Rapport Grønlands Geologiske Undersøgelse, p. 1–42.

Bons, P.D., Baur, A., Elburg, M.A., Lindhuber, M.J., Marks, M.A.W., Soesoo, A., Van Milligen, B.P., and Walte, N.P., 2015, Layered intrusions and traffic jams: Geology, v. 43, p. 71–74, doi:10.1130/G36276.1.

Boorman, S., Boudreau, A., and Kruger, F.J., 2004, The Lower Zone-Critical Zone transition of the Bushveld Complex: A quantitative textural study: Journal of Petrology, v. 45, p. 1209–1235, doi:10.1093/petrology/egh011.

Borradaile, G., 1987, Anisotropy of magnetic susceptibility: rock composition versus strain: Tectonophysics, v. 138, p. 327–329, doi:10.1016/0040-1951(87)90051-5.

Borradaile, G.J., 1988, Magnetic susceptibility, petrofabrics and strain: Tectonophysics, v. 156, p. 1–20, doi:10.1016/0040-1951(88)90279-X.

Borradaile, G.J., and Gauthier, D., 2001, AMS-detection of inverse fabrics without AARM, in ophiolite dikes: Geophysical Research Letters, v. 28, p. 3517–3520, doi:10.1029/2001GL012976.

Borradaile, G.J., and Henry, B., 1997, Tectonic Applications of Magnetic Susceptibility and its Anisotropy: Earth-Science Reviews, v. 42, p. 49–93, doi:10.1016/S0012-8252(96)00044-X.

Borradaile, G.J., and Jackson, M., 2004, Anisotropy of magnetic susceptibility (AMS): Magnetic petrofabrics of deformed rocks: Geological Society Special Publication, v. 238, p. 299–360, doi:10.1144/GSL.SP.2004.238.01.18.

Borradaile, G., Keeler, W., Alford, C., and Sarvas, P., 1987, Anisotropy of magnetic susceptibility of some metamorphic minerals: Physics of the Earth and Planetary Interiors, v. 48, p. 161–166, doi:10.1016/0031-9201(87)90119-1.

Borst, A.M., Friis, H., Andersen, T., Nielsen, T.F.D., Waight, T.E., and Smit, M.A., 2016, Zirconosilicates in the kakortokites of the Ilímaussaq complex, South Greenland: Implications for fluid evolution and high-field-strength and rare-earth element mineralization in agpaitic systems: Mineralogical Magazine, v. 80, p. 5–30, doi:10.1180/minmag.2016.080.046.

Borst, A.M., Friis, H., Nielsen, T.F.D., and Waight, T.E., 2018, Bulk and mush melt evolution in agpaitic intrusions: Insights from compositional zoning in eudialyte, Ilímaussaq complex, South Greenland: Journal of Petrology, v. 59, p. 589–612, doi:10.1093/petrology/egy038.

Borst, A.M., Waight, T.E., Finch, A.A., Storey, M., and Roux, P.J.L., 2019, Dating agpaitic rocks: A multi-system (U/Pb, Sm/Nd, Rb/Sr and 40Ar/39Ar) isotopic study of layered nepheline syenites from the Ilímaussaq complex, Greenland: Lithos, v. 324–325, p. 74–88, doi:10.1016/j.lithos.2018.10.037.

Boudreau, A.E., 1988, Investigations of the Stillwater Complex. IV. The role of volatiles in the petrogenesis of the J-M Reef, Minneapolis adit sction: Canadian Mineralogist, v. 26, p. 193–208, https://www.researchgate.net/publication/284801885.

Boudreau, A.E., and McBirney, A.R., 1997, The Skaergaard Layered Series. Part III. Non-dynamic Layering: Journal of Petrology, v. 38, p. 1003–1020, doi:10.1093/petroj/38.8.1003.

Branagan, D.F., 2005, History of Geology from 1900 to 1962, *in* Encyclopedia of Geology, p. 185–196, doi:10.1016/B0-12-369396-9/00370-1.

Burton-Johnson, A., Macpherson, C.G., Muraszko, J.R., Harrison, R.J., and Jordan, T.A., 2019, Tectonic strain recorded by magnetic fabrics (AMS) in plutons, including Mt Kinabalu, Borneo: A tool to explore past tectonic regimes and syn-magmatic deformation: Journal of Structural Geology, v. 119, p. 50–60, doi:10.1016/j.jsg.2018.11.014.

Černý, J., Melichar, R., Všianský, D., and Drahokoupil, J., 2020, Magnetic Anisotropy of Rocks: A New Classification of Inverse Magnetic Fabrics to Help Geological Interpretations: Journal of Geophysical Research: Solid Earth, v. 125, p. 1–13, doi:10.1029/2020JB020426.

Chadwick, B., and Garde, A.A., 1996, Palaeoproterozoic oblique plate convergence in South Greenland: a reappraisal of the Ketilidian Orogen: Geological Society Special Publication, v. 112, p. 179–196.

Clark, D.A., 1997, Magnetic petrophysics and magnetic petrology: aids to geological interpretation of magnetic surveys: Journal of Australian Geology & Geophysics, v. 17, p. 83–103.

Duchesne, J.C., and Charlier, B., 2005, Geochemistry of cumulates from the Bjerkreim-Sokndal layered intrusion (S. Norway). Part I: Constraints from major elements on the mechanism of cumulate formation and on the jotunite liquid line of descent: Lithos, v. 83, p. 229–254, doi:10.1016/j.lithos.2005.03.004.

Dunlop, D.J., and Özdemir, Ö., 1997, Rock Magnetism: 1–565 p.

Eales, H. V, and Cawthorn, R.G., 1996, The Bushveld Complex, *in* Layered Intrusions, p. 181–229.

Ferré, E.C., 2002, Theoretical models of intermediate and inverse AMS fabrics: Geophysical Research Letters, v. 29, p. 1–4, doi:10.1029/2001GL014367.

Ferré, E.C., Maes, S.M., and Butak, K.C., 2009, The magnetic stratification of layered mafic intrusions: Natural examples and numerical models: Lithos, v. 111, p. 83–94, doi:10.1016/j.lithos.2009.03.042.

Ferré, E.C., Michelsen, K.J., Ernst, W.G., Boyd, J.D., and Canon-Tapia, E., 2012, Vertical zonation of the Barcroft granodiorite, White Mountains, California: Implications for magmatic processes: American Mineralogist, v. 97, p. 1049–1059, doi:10.2138/am.2012.4013.

Garde, A.A., Hamilton, M.A., Chadwick, B., Grocott, J., and McCaffrey, K.J.W., 2002, The Ketilidian orogen of South Greenland: Geochronology, tectonics, magmatism, and fore-arc accretion during Palaeoproterozoic oblique convergence: Canadian Journal of Earth Sciences, v. 39, p. 765–793, doi:10.1139/e02-026.

Gordon, S.G., 1927, On Arfvedsonite, Riebeckite, and Crocidolite from Greenland: Proceedings of the Academy of Natural Sciences of Philadelphia, v. 79, p. 193–205.

Hess, H.H., 1960, Stillwater Igneous Complex, Montana: GSA Memoirs, v. 80, p. 1–225, doi:10.1130/MEM80.

Higgins, M.D., 2011, Textural coarsening in igneous rocks: International Geology Review, v. 53, p. 354–376, doi:10.1080/00206814.2010.496177.

Higgins, M.D., 1991, The origin of laminated and massive anorthosite, Sept Iles layered intrusion, Quebec, Canada: Contributions to Mineralogy and Petrology, v. 106, p. 340–354.

Hogarth, D.D., Chao, G.Y., and Townsend, M.G., 1987, Potassium- and fluorine-rich amphiboles from the Gatineau area, Quebec: Canadian Mineralogist, v. 25, p. 739–753.

Holness, M.B., 2018, Melt segregation from silicic crystal mushes: a critical appraisal of possible mechanisms and their microstructural record: Contributions to Mineralogy and Petrology, v. 173, doi:10.1007/s00410-018-1465-2.

Holness, M.B., 2014, The effect of crystallization time on plagioclase grain shape in dolerites: Contributions to Mineralogy and Petrology, v. 168, p. 1–19, doi:10.1007/s00410-014-1076-5.

Holness, M.B., Sides, R., Prior, D.J., Cheadle, M.J., and Upton, B.G.J., 2012, The peridotite plugs of Rum: Crystal settling and fabric development in magma conduits: Lithos, v. 134–135, p. 23–40, doi:10.1016/j.lithos.2011.11.024.

Holness, M.B., Vukmanovic, Z., and Mariani, E., 2017, Assessing the role of compaction in the formation of adcumulates: A microstructural perspective: Journal of Petrology, v. 58, p. 643–674, doi:10.1093/petrology/egx037.

Holness, M.B., Vukmanovic, Z., and O'Driscoll, B., 2023, The Formation of Chromite Chains and Clusters in Igneous Rocks: Journal of Petrology, v. 64, doi:10.1093/petrology/egac124.

Hunt, E.J., Finch, A.A., and Donaldson, C.H., 2017, Layering in peralkaline magmas, Ilímaussaq Complex, S Greenland: Lithos, v. 268–271, p. 1–15, doi:10.1016/j.lithos.2016.10.023.

Irvine, T.N., 1980, Magmatic infiltration metasomatism, double-diffusive fractional crystallization, and adcumulus growth in the Muskox intrusion and other layered intrusions, *in* Physics of Magmatic Processes, p. 325–383, doi:10.1515/9781400854493.325.

Jackson, M., 1991, Anisotropy of magnetic remanence: A brief review of mineralogical sources, physical origins, and geological applications, and comparison with susceptibility anisotropy: Pure and Applied Geophysics, v. 36, p. 1–28, doi:10.1007/BF00878885.

Jackson, E., 1961, Primary textures and mineral associations in the ultramafic zone of the Stillwater Complex: Geological Survey Professional Paper, p. 1–103, doi:10.3133/pp358.

Jelinek, V., 1981, Characterization of the magnetic fabric of rocks: Tectonophysics, v. 79, p. 63–67.

Jelinek, V., 1977, The statistical theory of measuring anisotropy of magnetic susceptibility of rocks and its application, *in* Brno: Geofyzika, p. 1–88.

Knight, M.D., and Walker, G.P.L., 1988, Magma flow directions in dikes of the Koolau complex, Oahu, determined from magnetic fabric studies: Journal of Geophysical Research, v. 93, p. 4301–4319, doi:10.1029/JB093iB05p04301.

Koopmans, L., McCarthy, W., and Magee, C., 2022, Dyke architecture, mineral layering, and magmatic convection; New perspectives from the Younger Giant Dyke Complex, S Greenland: Geochemistry, Geophysics, Geosystems, v. 23, doi:10.1029/2021GC010260.

Kruger, W., and Latypov, R., 2022, In situ crystallization of non-cotectic and foliated igneous rocks on a magma chamber floor: Communications Earth and Environment, v. 3, p. 1–12, doi:10.1038/s43247-022-00584-6.

Krumrei, T. V., Villa, I.M., Marks, M.A.W., and Markl, G., 2006, A 40Ar/39Ar and U/Pb isotopic study of the Ilímaussaq complex, South Greenland: Implications for the 40K decay constant and for the duration of magmatic activity in a peralkaline complex: Chemical Geology, v. 227, p. 258–273, doi:10.1016/j.chemgeo.2005.10.004.

Larsen, L.M., and Sørensen, H., 1987, The llímaussaq intrusion - progressive crystallization and formation of layering in an agpaitic magma: Geological Society Special Publication, v. 30, p. 473–488, http://sp.lyellcollection.org/.

Latimer, B., McCarthy, W., Mattsson, T., and Reavy, J., 2024, Enclaves as mushy magma strain archives: New perspectives on composite magmatic fabrics in plutons: Geosphere, doi:10.1130/ges02786.1.

Latypov, R., Chistyakova, S., Barnes, S.J., and Hunt, E.J., 2017, Origin of platinum deposits in layered intrusions by in situ crystallization: Evidence from undercutting Merensky Reef of the Bushveld Complex: Journal of Petrology, v. 58, p. 715–762, doi:10.1093/petrology/egx032.

Lindhuber, M.J., Marks, M.A.W., Bons, P.D., Wenzel, T., and Markl, G., 2015, Crystal mat-formation as an igneous layering-forming process: Textural and geochemical evidence from the "lower layered" nepheline syenite sequence of the Ilímaussaq complex, South Greenland: Lithos, v. 224–225, p. 295–309, doi:10.1016/j.lithos.2015.03.007.

Lofgren, G.E., and Donaldson, C.H., 1975, Curved Branching Crystals and Differentiation in Comb-Layered Rocks: Contributions to Mineralogy and Petrology, v. 49, p. 309–319, doi:10.1007/BF00376183.

Maes, S.M., Ferré, E.C., Tikoff, B., Brown, P.E., and Marsh, J.S., 2008, Rock magnetic stratigraphy of a mafic layered sill: A key to the Karoo volcanics plumbing system: Journal of Volcanology and Geothermal Research, v. 172, p. 75–92, doi:10.1016/j.jvolgeores.2005.07.038.

Magee, C., O'Driscoll, B., Petronis, M.S., and Stevenson, C.T.E., 2016, Three-dimensional magma flow dynamics within subvolcanic sheet intrusions: Geosphere, v. 12, p. 842–866, doi:10.1130/GES01270.1.

Mangler, M.F., Humphreys, M.C.S., Wadsworth, F.B., Iveson, A.A., and Higgins, M.D., 2022, Variation of plagioclase shape with size in intermediate magmas: a window into incipient plagioclase crystallisation: Contributions to Mineralogy and Petrology, v. 177, doi:10.1007/s00410-022-01922-9.

Marks, M.A.W., Hettmann, K., Schilling, J., Frost, B.R., and Markl, G., 2011, The mineralogical diversity of alkaline igneous rocks: Critical factors for thetransition from miaskitic to agpaitic phase assemblages: Journal of Petrology, v. 52, p. 439–455, doi:10.1093/petrology/egq086.

Marks, M.A.W., and Markl, G., 2015, The Ilímaussaq Alkaline Complex, South Greenland, *in* Layered Intrusions, Springer, p. 649–691, doi:10.1007/978-94-017-9652-1_14.

Martín-Hernández, F., Lüneburg, C.M., Aubourg, C., and Jackson, M., 2004, Magnetic fabric: Methods and applications - An introduction: Geological Society Special Publication, v. 238, p. 1–7, doi:10.1144/GSL.SP.2004.238.01.01.

Mattsson, T., Petri, B., Almqvist, B., McCarthy, W., Burchardt, S., Palma, J.O., Hammer, Ø., and Galland, O., 2021, Decrypting magnetic fabrics (AMS, AARM, AIRM) through the analysis of mineral shape fabrics and distribution anisotropy: Journal of Geophysical Research: Solid Earth, v. 126, doi:10.1029/2021JB021895.

McCarthy, W., Reavy, R.J., Stevenson, C.T., and Petronis, M.S., 2015, Late Caledonian transpression and the structural controls on pluton construction; New insights from the Omey Pluton, western Ireland: Earth and Environmental Science Transactions of the Royal Society of Edinburgh, v. 106, p. 11–28, doi:10.1017/S1755691015000201.

Meurer, W.P., and Boudreau, A.E., 1998, Compaction of Igneous Cumulates Part II: Compaction and the Development of Igneous Foliations: The Journal of Geology, v. 106, p. 293–304, doi:10.1086/516023.

Namur, O. et al., 2015, Igneous Layering in Basaltic Magma Chambers, *in* Layered Intrusions, p. 75–152, doi:10.1007/978-94-017-9652-1_2.

Naslund, H.R., and McBirney, A.R., 1996, Mechanisms of Formation of Igneous Layering, *in* Layered Intrusions, p. 1–43.

Nielsen, T.F.D., Andersen, J.C.Ø., Holness, M.B., Keiding, J.K., Rudashevsky, N.S., Rudashevsky, V.N., Salmonsen, L.P., Tegner, C., and Veksler, I. V., 2015, The skaergaard PGE and gold deposit: The result of in situ fractionation, sulphide saturation, and magma chamber-scale precious metal redistribution by immiscible Fe-rich melt: Journal of Petrology, v. 56, p. 1643–1676, doi:10.1093/petrology/egv049.

O'Driscoll, B., Donaldson, C.H., Troll, V.R., Jerram, D.A., and Emeleus, C.H., 2007, An origin for harrisitic and granular olivine in the rum layered suite, NW Scotland: A crystal size distribution study: Journal of Petrology, v. 48, p. 253–270, doi:10.1093/petrology/egl059.

O'Driscoll, B., Ferré, E.C., Stevenson, C.T.E., and Magee, C., 2015, The Significance of Magnetic Fabric in Layered Mafic-Ultramafic Intrusions, *in* Layered Intrusions, Springer, p. 295–329, doi:10.1007/978-94-017-9652-1_7.

O'Driscoll, B., Petronis, M.S., Marks, M.A.W., Mccarthy, W.S., Mariani, E., Stevenson, C.T.E., Clay, P.L., and Geissman, J.W., 2024, Magnetic Fabrics in Laminated Rocks of the Ilímaussaq Igneous Complex, Southern Greenland: The Canadian Journal of Mineralogy and Petrology, doi:10.3749/2400008.

O'Driscoll, B., Stevenson, C.T.E., and Troll, V.R., 2008, Mineral lamination development in layered gabbros of the british palaeogene igneous province: A combined anisotropy of magnetic susceptibility, quantitative textural and mineral chemistry study: Journal of Petrology, v. 49, p. 1187–1221, doi:10.1093/petrology/egn022.

O'Driscoll, B., and Van Tongeren, J.A., 2017, Layered intrusions: From petrological paradigms to precious metal repositories: Elements, v. 13, p. 383–389, doi:10.2138/gselements.13.6.383.

Pang, K.N., Li, C., Zhou, M.F., and Ripley, E.M., 2009, Mineral compositional constraints on petrogenesis and oxide ore genesis of the late Permian Panzhihua layered gabbroic intrusion, SW China: Lithos, v. 110, p. 199–214, doi:10.1016/j.lithos.2009.01.007.

Parés, J.M., 2015, Sixty years of anisotropy of magnetic susceptibility in deformed sedimentary rocks: Frontiers in Earth Science, v. 3, doi:10.3389/feart.2015.00004.

Petronis, M.S., O'Driscoll, B., Stevenson, C.T.E., and Reavy, R.J., 2012, Controls on emplacement of the Caledonian Ross of Mull Granite, NW Scotland: Anisotropy of magnetic susceptibility and magmatic and regional structures: Bulletin of the Geological Society of America, v. 124, p. 906–927, doi:10.1130/B30362.1.

Pfaff, K., Krumrei, T., Marks, M., Wenzel, T., Rudolf, T., and Markl, G., 2008, Chemical and physical evolution of the "lower layered sequence" from the nepheline syenitic Ilímaussaq intrusion, South Greenland: Implications for the origin of magmatic layering in peralkaline felsic liquids: Lithos, v. 106, p. 280–296, doi:10.1016/j.lithos.2008.07.018.

Ratschbacher, B.C., Marks, M.A.W., Bons, P.D., Wenzel, T., and Markl, G., 2015, Emplacement and geochemical evolution of highly evolved syenites investigated by a combined structural and geochemical field study: The lujavrites of the Ilímaussaq complex, SW Greenland: Lithos, v. 231, p. 62–76, doi:10.1016/j.lithos.2015.06.004.

Rosenblum, S., and Brownfield, I.K., 2000, Magnetic Susceptibility of Minerals.:

Schønwandt, H.K., Barnes, G.B., and Ulrich, T., 2016, A Description of the World-Class Rare Earth Element Deposit, Tanbreez, South Greenland, *in* Rare Earths Industry: Technological, Economic, and Environmental Implications, Elsevier Inc., p. 73–85, doi:10.1016/B978-0-12-802328-0.00005-X.

Selkin, P.A., Gee, J.S., and Meurer, W.P., 2014, Magnetic anisotropy as a tracer of crystal accumulation and transport, Middle Banded Series, Stillwater Complex, Montana: Tectonophysics, v. 629, p. 123–137, doi:10.1016/j.tecto.2014.03.028.

Smith, W.D., and Maier, W.D., 2021, The geotectonic setting, age and mineral deposit inventory of global layered intrusions: Earth-Science Reviews, v. 220, p. 1–36, doi:10.1016/j.earscirev.2021.103736.

Sørensen, H., 2001, Brief introduction to the geology of the Ilímaussaq alkaline complex, South Greenland, and its exploration history: Geology of Greenland Survey Bulletin, v. 190, p. 7–23, doi:10.34194/ggub.v190.5170.

Sørensen, H., Bailey, J.C., and Rose-Hansen, J., 2011, The emplacement and crystallization of the U-TH-REE-rich agpaitic and hyperagpaitic lujavrites at Kvanefjeld, Ilímaussaq alkaline complex, South Greenland: Bulletin of the Geological Society of Denmark, v. 59, p. 69–92, doi:10.37570/bgsd-2011-59-08.

Sørensen, H., Bohse, H., and Bailey, J.C., 2006, The origin and mode of emplacement of lujavrites in the Ilímaussaq alkaline complex, South Greenland: Lithos, v. 91, p. 286–300, doi:10.1016/j.lithos.2006.03.021.

Tait, S., and Jaupart, C., 1992, Compositional convection in a reactive crystalline mush and melt differentiation: Journal of Geophysical Research, v. 97, p. 6735–6756, doi:10.1029/92JB00016.

Tarling, D.H. (Donald H., and Hrouda, F. (František), 1993, The magnetic anisotropy of rocks: Chapman & Hall, 1–213 p.

Upton, B.G.J., 2013a, Tectono-magmatic evolution of the younger Gardar southern rift, South Greenland: Geological Survey of Denmark and Greenland Bulletin, v. 29, p. 1–116, doi:10.34194/geusb.v29.4692.

Upton, B.G.J., 2013b, Tectono-magmatic evolution of the younger Gardar southern rift, South Greenland: Geological Survey of Denmark and Greenland Bulletin, v. 29, p. 1–124.

Upton, B.G.J., Emeleus, C.H., Heaman, L.M., Goodenough, K.M., and Finch, A.A., 2003, Magmatism of the mid-Proterozoic Gardar Province, South Greenland: Chronology, petrogenesis and geological setting: Lithos, v. 68, p. 43–65, doi:10.1016/S0024-4937(03)00030-6.

Vukmanovic, Z., Holness, M.B., Stock, M.J., and Roberts, R.J., 2019, The Creation and Evolution of Crystal Mush in the Upper Zone of the Rustenburg Layered Suite, Bushveld Complex, South Africa: Journal of Petrology, v. 60, p. 1523–1542, doi:10.1093/petrology/egz038.

Wager, L.R., Brown, G.M., and Wadsworth, W.J., 1960, Types of Igneous Cumulates: Journal of Petrology, v. 1, p. 73–85, http://petrology.oxfordjournals.org/.

Wieser, P.E., Vukmanovic, Z., Kilian, R., Ringe, E., Holness, M.B., Maclennan, J., and Edmonds, M., 2019, To sink, swim, twin, or nucleate: A critical appraisal of crystal aggregation processes: Geology, v. 47, p. 948–952, doi:10.1130/G46660.1.

Young, I.M., and Donaldson, C.H., 1985, Formation of granular-textured layers and laminae within the Rhum crystal pile: Geological Magazine, v. 122, p. 519–528, doi:10.1017/S0016756800035433.

Žák, J., Schulmann, K., and Hrouda, F., 2005, Multiple magmatic fabrics in the Sázava pluton (Bohemian Massif, Czech Republic): A result of superposition of wrench-dominated regional transpression on final emplacement: Journal of Structural Geology, v. 27, p. 805–822, doi:10.1016/j.jsg.2005.01.012.

Zhang, B., Hu, X., Asimow, P.D., Zhang, X., Xu, J., Zhou, W., and Fan, D., 2019, Crystal size distribution of amphibole grown from hydrous basaltic melt at 0.6-2.6 GPa and 860-970 °c: American Mineralogist, v. 104, p. 525–535, doi:10.2138/am-2019-6759.

Figure Captions

Fig. 1 (a) Schematic cross-section through the Ilímaussaq complex, modified after Borst et al. (2018) and Andersen et al., (1981). (b) Geological map of the Ilímaussaq complex, modified after Upton (2013), with locations of REE deposits marked with red diamonds. Labels '1' and '2' mark the locations of the two study areas, Laksetværelv and Kringlerne respectively. (c) Panoramic photograph of the lower layered kakortokites, with units 0 through +12 labelled. Blue dotted lines highlight the layers deflecting around the autolith.

Fig. 2 Schematic diagrams of (a) open system model based on description by Hunt et al. (2017); (b) closed system model based on description by Borst et al. (2018), Bons et al. (2015), and Lindhuber et al. (2015).

Fig. 3 Predicted rock fabrics (random crystal orientations, R = grey; crystal foliation, F = blue) in layers formed from different layering models as described by Hunt et al. (2017), Borst et al. (2018), Lindhuber et al. (2015), and Bons et al. (2015).

Fig. 4 (a) Photograph of Locality 1; (b) Annotated photograph of Locality 1 with layer interpretation, layer labels, and sample locations (yellow squares); (c) Photograph of Locality 2; (d) Annotated photograph of Locality 2. Both localities are shown on the geological map in Fig. 1.

Fig. 5 (a) Relationship between crystallographic and magnetic susceptibility axes for normal and inverse AMS fabrics adapted from Ferré (2002); (b) Example prolate and oblate spheroids.

Fig. 6 (a) Panoramic photograph of kakortokite layers showing a bowl-like morphology with the base of black layers highlighted in blue; (b) Photograph of layer -1W/layer 0B boundary at Locality 1 and annotated of photograph, with alkali feldspar outlined; (c) Photograph of roof autolith (outlined in white) within kakortokites. Kakortokite layering can be seen deflecting above and below the autolith. The bases of black layers are highlighted in blue; (d) Structural map of the lower layered kakortokites with locations of photos a, b, and c marked. Geological map modified after Andersen et al. (1988) and Upton (2013).

Fig. 7 Geological field logs from Localities 1 and 2 in the kakortokites.

Fig. 8 (a) Photograph of kinked alkali feldspar within layer 0B at Locality 1; (b) XPL thin section image of kinked alkali felspar from layer -1W at Locality 1; (c) Photograph of layer 0B at Locality 1, with mineral foliation defined by alkali feldspar; (d) XPL thin section image of foliated alkali feldspar within intercumulus arfvedsonite in layer 0B, Locality 1; (e) Photograph of arfvedsonite oikocrysts within layer 0W at Locality 2; (f) PPL thin section image of arfvedsonite oikocryst with nepheline inclusions; (g) Photograph of aligned arfvedsonite in layer +2R at Locality 2; (h) Annotated photograph of aligned arfvedsonite (highlighted in yellow) in layer +2R at Locality 2; (i) XPL thin section image of arfvedsonite replacing alkali feldspar in layer 0B, Locality 1; (j) XPL thin section image of intercumulus nepheline groundmass and deformed alkali feldspar at the base of layer 0W at Locality 1; (k) XPL thin section image of patchy zoning of arfvedsonite in layer 0B, Locality 1; (l) Photograph of cm-scale layering within kakortokites, with layering defined by higher modal abundance of arfvedsonite.

Fig. 9 (a) Results of temperature-susceptibility experiments from Locality 1, coloured black, red and white to correspond with the colour layer the sample is from; (b) Results of temperature-susceptibility experiments from Locality 2; (c) SIRM results; and (d) BIRM results. Duplicate SIRM and BIRM experiments were run on samples 65, 69, 75 and 77.

Fig. 10 Stratigraphic logs for Locality 1 (left) and Locality 2 (right). Plotted adjacent to the logs are mean susceptibility (K_{mean}) in blue, AMS degree of anisotropy (P_j) in pink, and AMS shape factor (T) in red. Top left: T vs P_j polar plot, with each point representing the average T and P_j data from a sample site. All sample sites from both localities are plotted.

Fig. 11 AMS and AARM data from Locality 1 (left) and Locality 2 (right), N stands for number of sub-specimens analysed per sample site. Stereonet A: average K_1 and K_3 data from each sample site at both localities, coloured by mean susceptibility. Contours are of K_3 data from black samples, showing that in black layers K_3 is typically orientated towards the NE. A progressive rotation of K_3 from NE to SE is observed as mean susceptibility decreases. Stereonet B: average K_1, K_2, and K_3 data from each sample site at both localities.

Fig. 12 Results of EBSD, AMS and AARM on representative samples from layers 0B (sample 65), 0R (sample 69) and 0W (sample 77) from Unit 0, and layer +2B (sample 24). EBSD data is plotted as pole figures of the relevant crystal planes for the main cumulus and intercumulus minerals in the kakortokites. EBSD pole figures are plotted in the ZX plane, displayed as equal area stereonets in the lower hemisphere, and reorientated to the geographic coordinate system for direct comparison with AMS and AARM data. CPO contour indicates multiples of random distribution. Modal layering attitude as measured in the field is displayed on each pole figure (orange plane). Schematic crystal shapes with CPO faces labelled are displayed at the base of the figure (these may not match the habits of the euhedral crystals that were present in the magma).

Fig. 13 (a) Structural map of the kakortokites showing where obliquity between mineral foliation and modal layering is recorded. Geological map modified after Andersen et al. (1988) and Upton (2013); (b) Schematic cross-section of Ilímaussaq adapted from Andersen et al. (1981) with proposed locations of our study localities marked; (c) Crystal mat model showing stages of development and the predicted mineral and magnetic fabrics that would be produced.

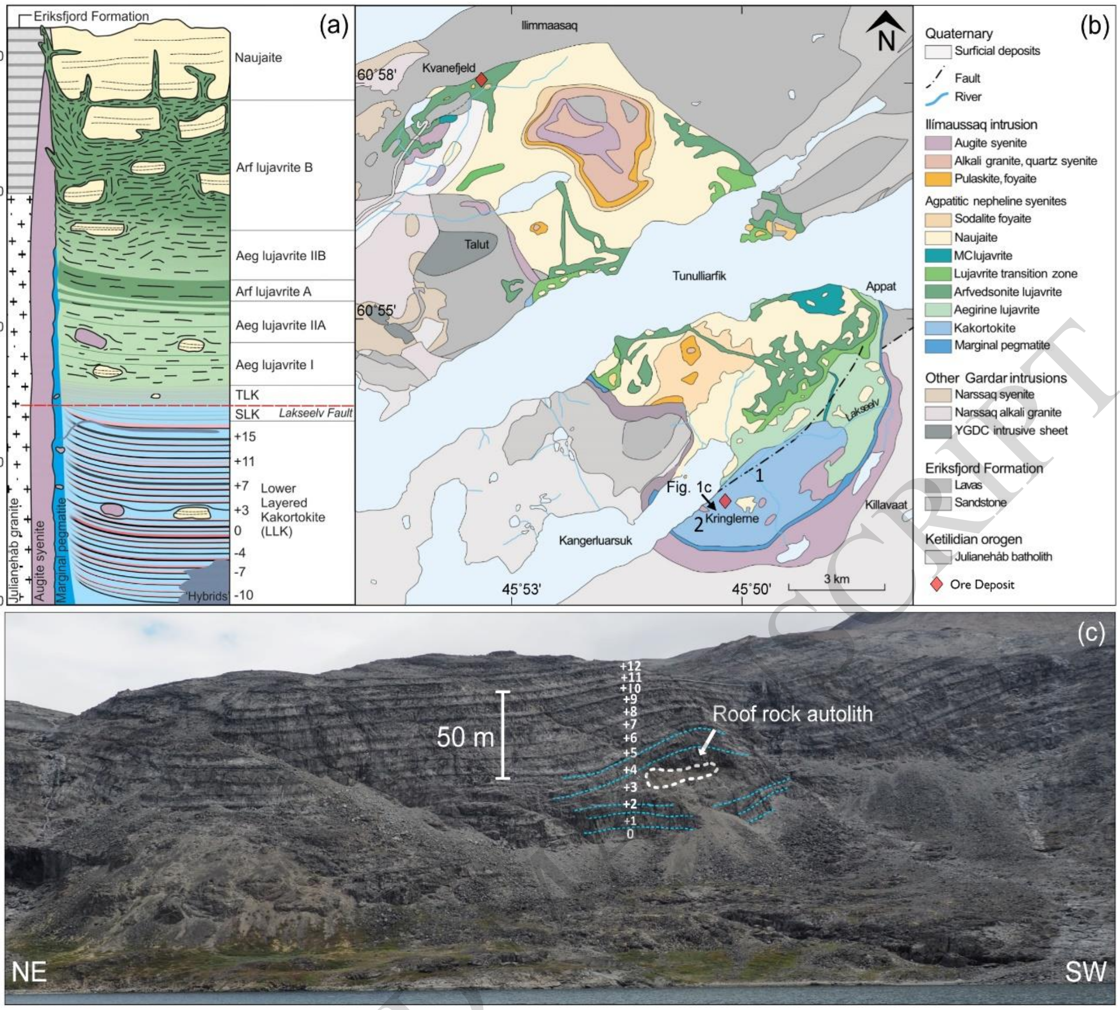
(a)
Eriksfjord Formation
Naujaite
Arf lujavrite B
Aeg lujavrite IIB
Arf lujavrite A
Aeg lujavrite IIA
Aeg lujavrite I
TLK
SLK
Lakseelv Fault
Lower Layered Kakortokite (LLK)
Hybrids
Julianehåb granite
Augite syenite
Marginal pegmatite
Height (m)
(b)
Ilimmaasaq
Kvanefjeld
Talut
Tunulliarfik
Appat
Lakseelv
Killavaat
Kringleme
Kangerluarsuk
Fig. 1c
3 km
Quaternary
Surficial deposits
Fault
River
Ilímaussaq intrusion
Augite syenite
Alkali granite, quartz syenite
Pulaskite, foyaite
Agpatitic nepheline syenites
Sodalite foyaite
Naujaite
MC lujavrite
Lujavrite transition zone
Arfvedsonite lujavrite
Aegirine lujavrite
Kakortokite
Marginal pegmatite
Other Gardar intrusions
Narssaq syenite
Narssaq alkali granite
YGDC intrusive sheet
Eriksfjord Formation
Lavas
Sandstone
Ketilidian orogen
Julianehåb batholith
Ore Deposit
(c)
50 m
Roof rock autolith
NE
SW

Figure 1

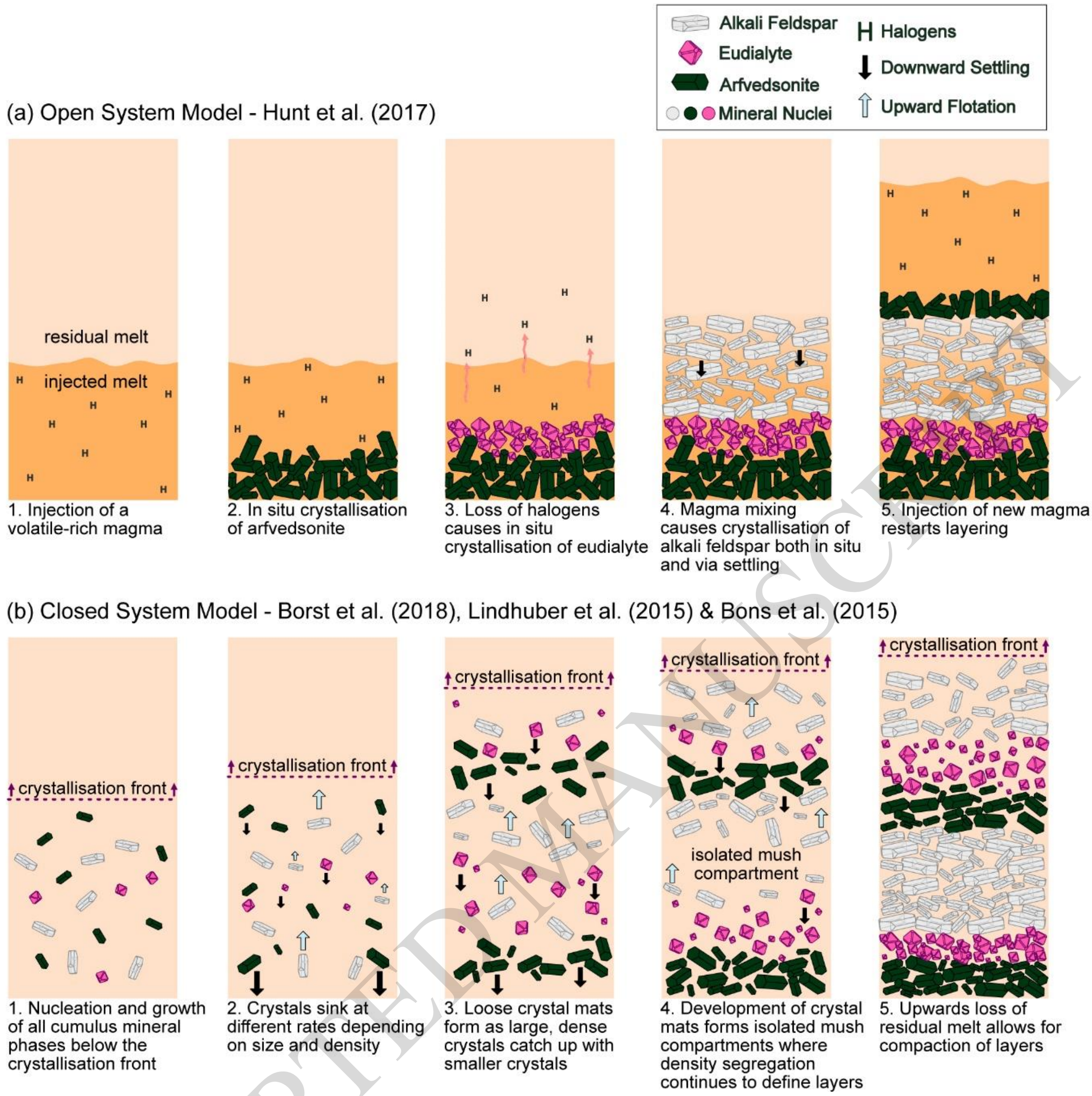
Alkali Feldspar
Eudialyte
Arfvedsonite
Mineral Nuclei
H Halogens
Downward Settling
Upward Flotation
(a) Open System Model - Hunt et al. (2017)
residual melt
injected melt
1. Injection of a volatile-rich magma
2. In situ crystallisation of arfvedsonite
3. Loss of halogens causes in situ crystallisation of eudialyte
4. Magma mixing causes crystallisation of alkali feldspar both in situ and via settling
5. Injection of new magma restarts layering
(b) Closed System Model - Borst et al. (2018), Lindhuber et al. (2015) & Bons et al. (2015)
crystallisation front
isolated mush compartment
1. Nucleation and growth of all cumulus mineral phases below the crystallisation front
2. Crystals sink at different rates depending on size and density
3. Loose crystal mats form as large, dense crystals catch up with smaller crystals
4. Development of crystal mats forms isolated mush compartments where density segregation continues to define layers
5. Upwards loss of residual melt allows for compaction of layers

Figure 2

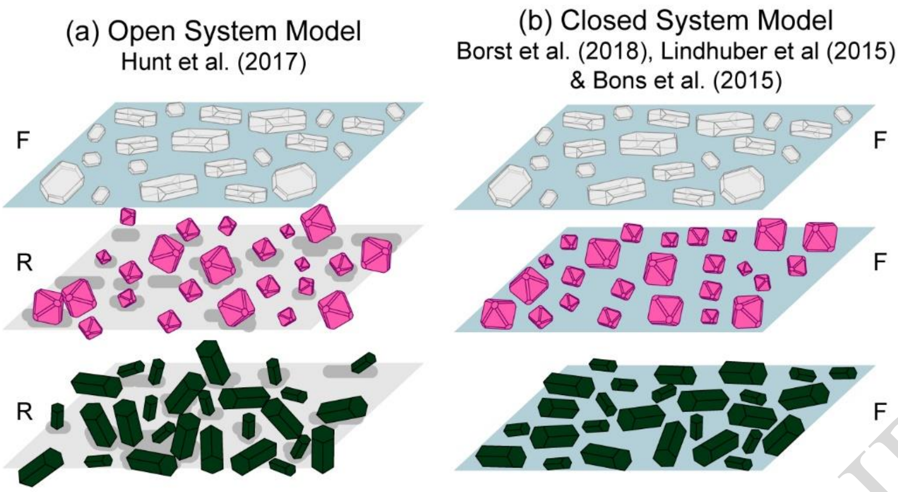

(a) Open System Model
Hunt et al. (2017)
(b) Closed System Model
Borst et al. (2018), Lindhuber et al (2015)
& Bons et al. (2015)
F
R
R
F
F
F

Figure 3

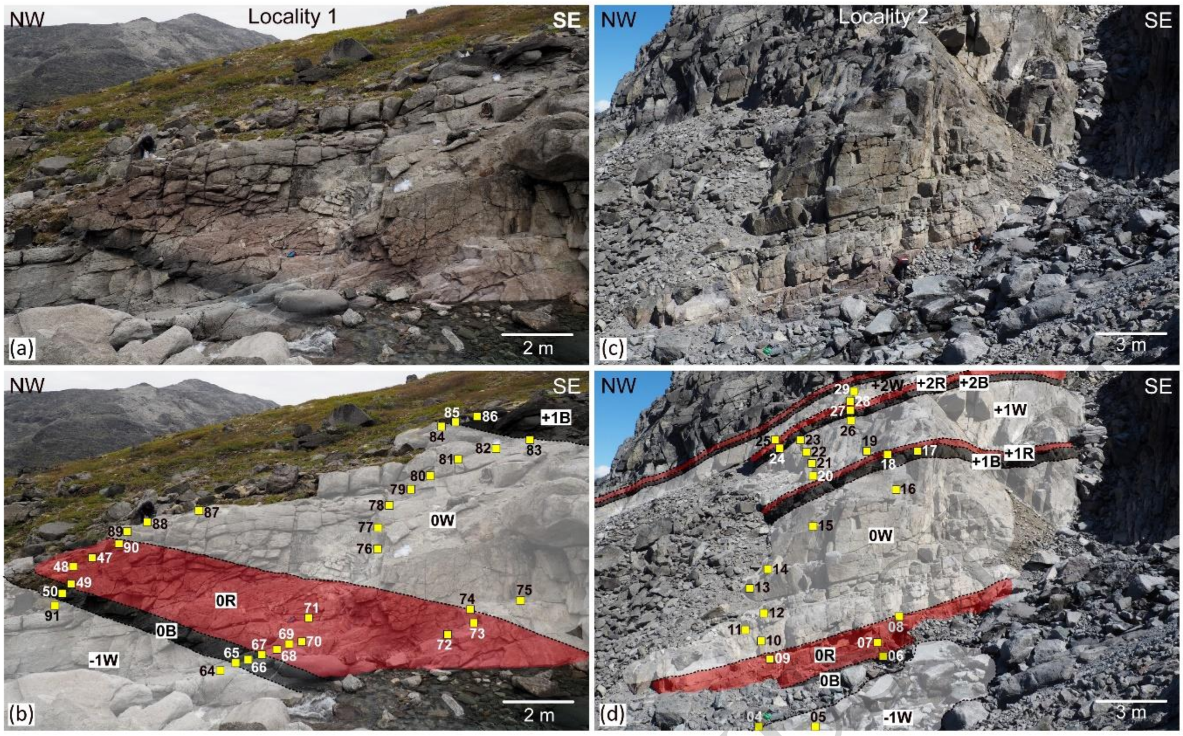

NW
Locality 1
SE
(a)
2 m
NW
Locality 2
SE
(c)
3 m
NW
SE
+1B
0W
0R
0B
-1W
(b)
2 m
NW
SE
+2W
+2R
+2B
+1W
+1R
+1B
0W
0R
0B
-1W
(d)
3 m

Figure 4

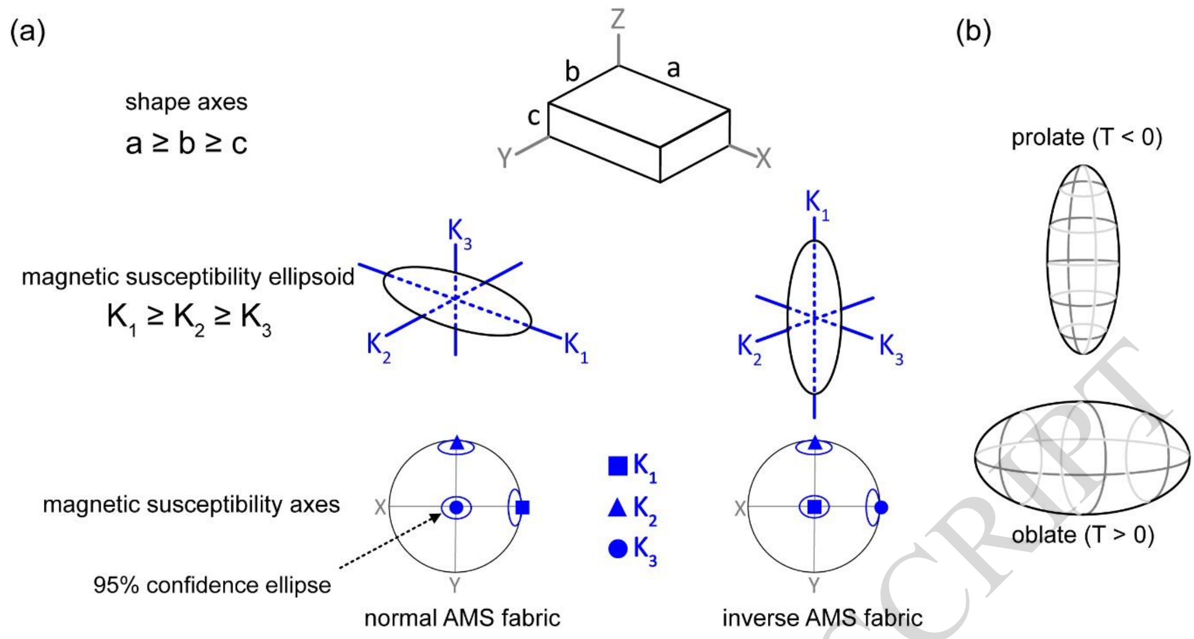
(a)
(b)
shape axes
a ≥ b ≥ c
Z
b
a
c
Y
X
prolate (T < 0)
magnetic susceptibility ellipsoid
K1 ≥ K2 ≥ K3
K3
K2
K1
K1
K2
K3
K1
K2
K3
magnetic susceptibility axes
95% confidence ellipse
X
Y
X
Y
oblate (T > 0)
normal AMS fabric
inverse AMS fabric

Figure 5

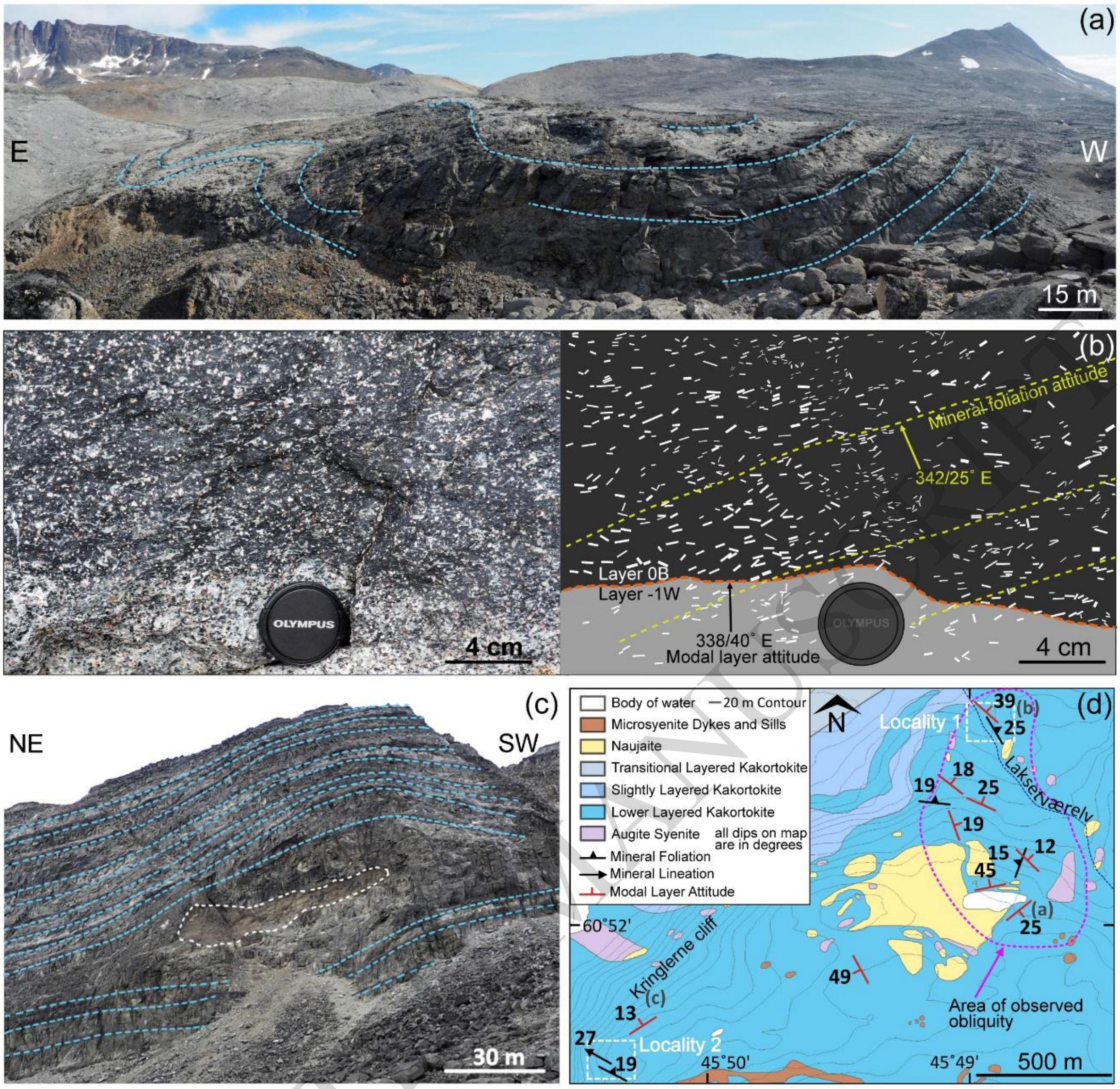

(a)
E
W
15 m
(b)
4 cm
Mineral foliation attitude
342/25° E
Layer 0B
Layer -1W
338/40° E
Modal layer attitude
4 cm
(c)
NE
SW
30 m
(d)
Body of water
20 m Contour
Microsyenite Dykes and Sills
Naujaite
Transitional Layered Kakortokite
Slightly Layered Kakortokite
Lower Layered Kakortokite
Augite Syenite
all dips on map are in degrees
Mineral Foliation
Mineral Lineation
Modal Layer Attitude
N
Locality 1
Lakseelv
Kringlerne cliff
Locality 2
60°52'
45°50'
45°49'
Area of observed obliquity
500 m

Figure 6

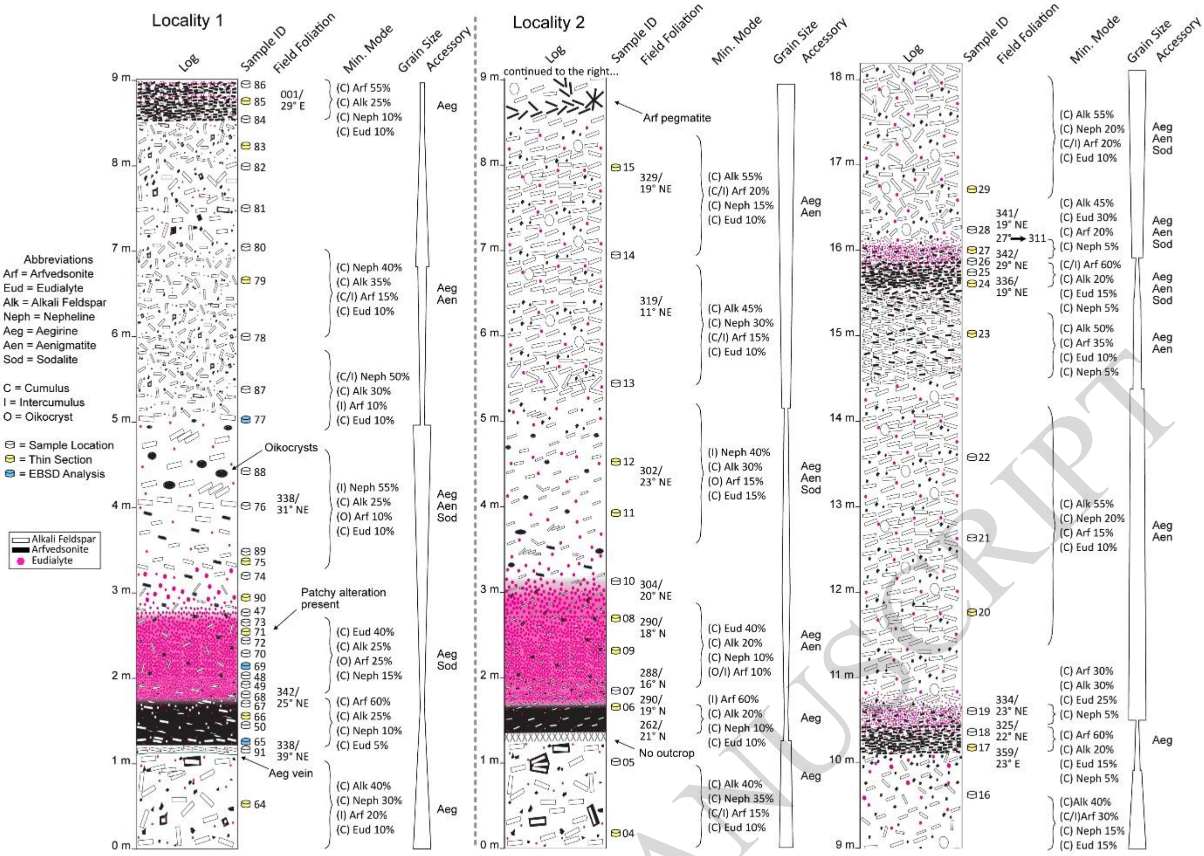
Locality 1
Locality 2
Log
Sample ID
Field Foliation
Min. Mode
Grain Size
Accessory
Abbreviations
Arf = Arfvedsonite
Eud = Eudialyte
Alk = Alkali Feldspar
Neph = Nepheline
Aeg = Aegirine
Aen = Aenigmatite
Sod = Sodalite
C = Cumulus
I = Intercumulus
O = Oikocryst
= Sample Location
= Thin Section
= EBSD Analysis
Alkali Feldspar
Arfvedsonite
Eudialyte
Oikocrysts
Patchy alteration present
Aeg vein
continued to the right...
Arf pegmatite
No outcrop

Figure 7

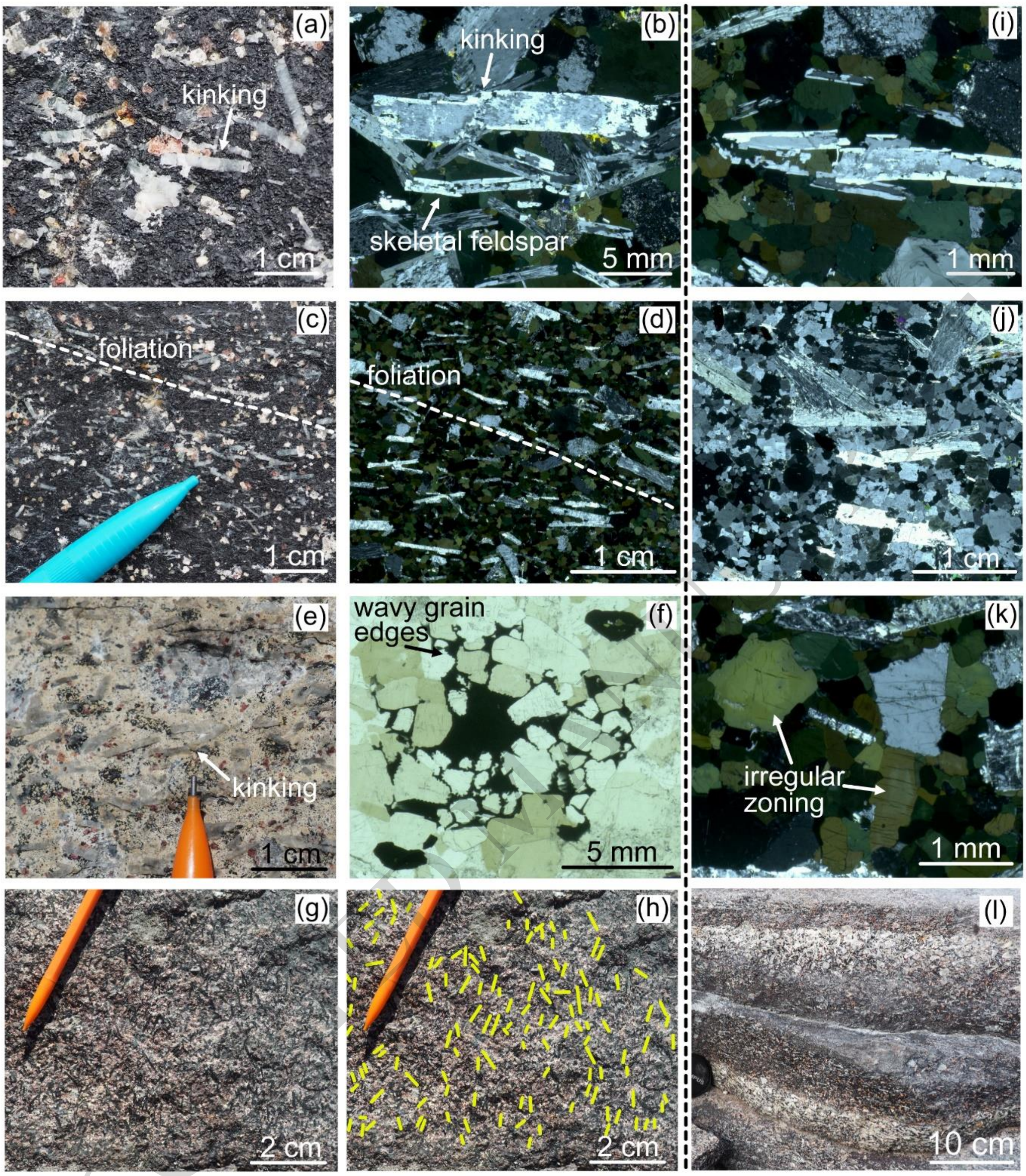
(a)
kinking
1 cm
(b)
kinking
skeletal feldspar
5 mm
(i)
1 mm
(c)
foliation
1 cm
(d)
foliation
1 cm
(j)
1 cm
(e)
kinking
1 cm
(f)
wavy grain edges
5 mm
(k)
irregular zoning
1 mm
(g)
2 cm
(h)
2 cm
(l)
10 cm

Figure 8

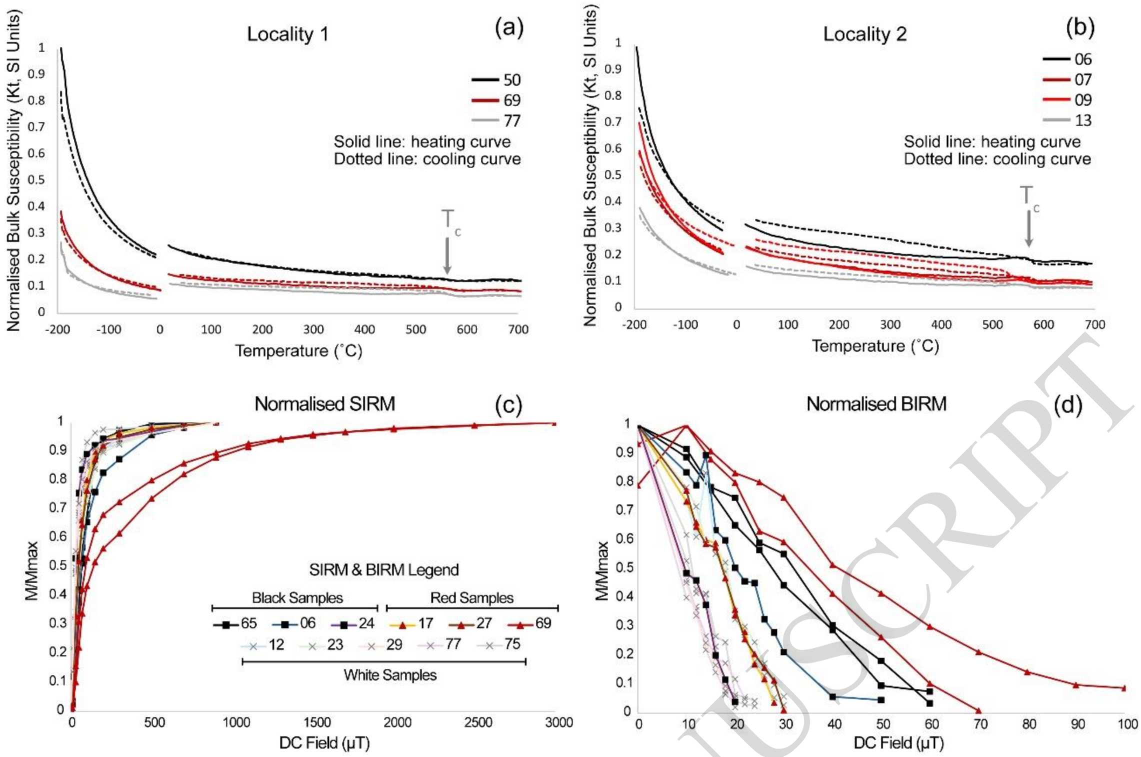

Locality 1
(a)
50
69
77
Solid line: heating curve
Dotted line: cooling curve
Tc
Normalised Bulk Susceptibility (Kt, SI Units)
Temperature (˚C)
Locality 2
(b)
06
07
09
13
Solid line: heating curve
Dotted line: cooling curve
Tc
Normalised Bulk Susceptibility (Kt, SI Units)
Temperature (˚C)
Normalised SIRM
(c)
M/Mmax
SIRM & BIRM Legend
Black Samples
Red Samples
65
06
24
17
27
69
12
23
29
77
75
White Samples
DC Field (μT)
Normalised BIRM
(d)
M/Mmax
DC Field (μT)

Figure 9

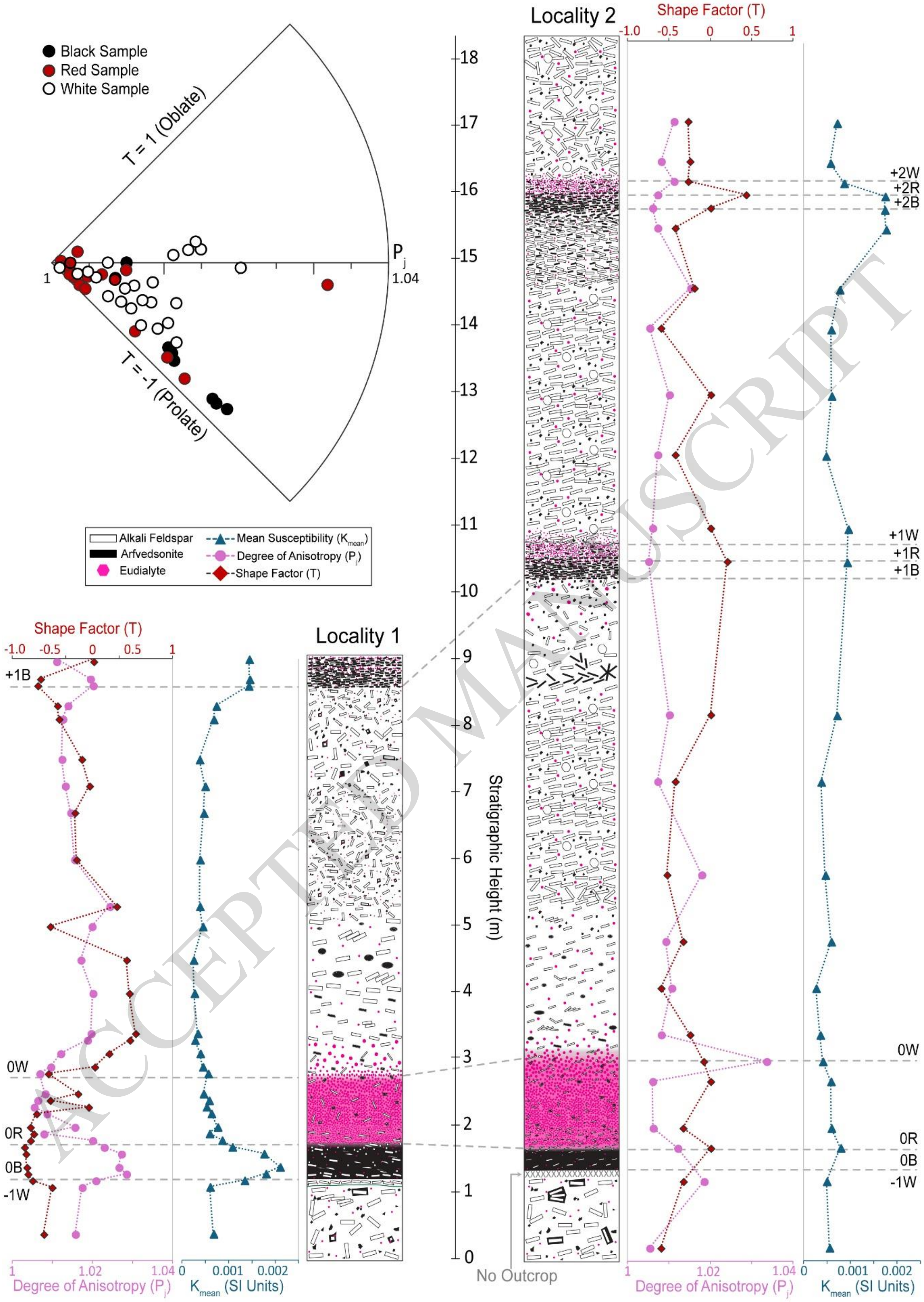

Black Sample
Red Sample
White Sample
T = 1 (Oblate)
T = -1 (Prolate)
Pj
1
1.04
Alkali Feldspar
Arfvedsonite
Eudialyte
Mean Susceptibility (Kmean)
Degree of Anisotropy (Pj)
Shape Factor (T)
Locality 1
Locality 2
Shape Factor (T)
-1.0 -0.5 0 0.5 1
Stratigraphic Height (m)
No Outcrop
+2W
+2R
+2B
+1W
+1R
+1B
0W
0R
0B
-1W
Degree of Anisotropy (Pj)
1 1.02 1.04
Kmean (SI Units)
0 0.001 0.002
ACCEPTED MANUSCRIPT

Figure 10

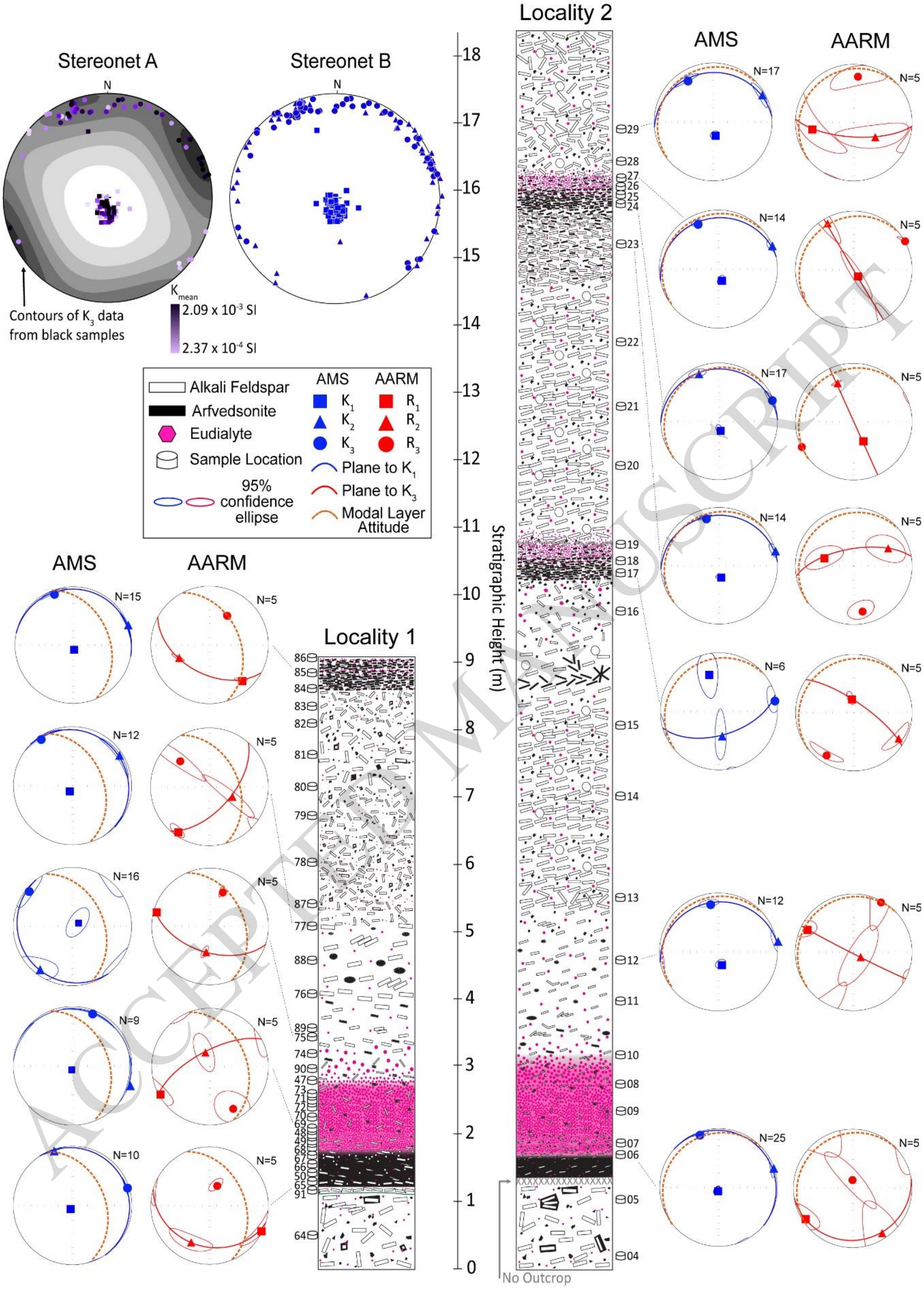
Stereonet A
N
Contours of K_3 data from black samples
K_{mean}
2.09 x 10^{-3} SI
2.37 x 10^{-4} SI
Stereonet B
N
Alkali Feldspar
Arfvedsonite
Eudialyte
Sample Location
95% confidence ellipse
AMS
AARM
K_1
K_2
K_3
R_1
R_2
R_3
Plane to K_1
Plane to K_3
Modal Layer Attitude
Locality 1
Locality 2
Stratigraphic Height (m)
No Outcrop
AMS
AARM

Figure 11

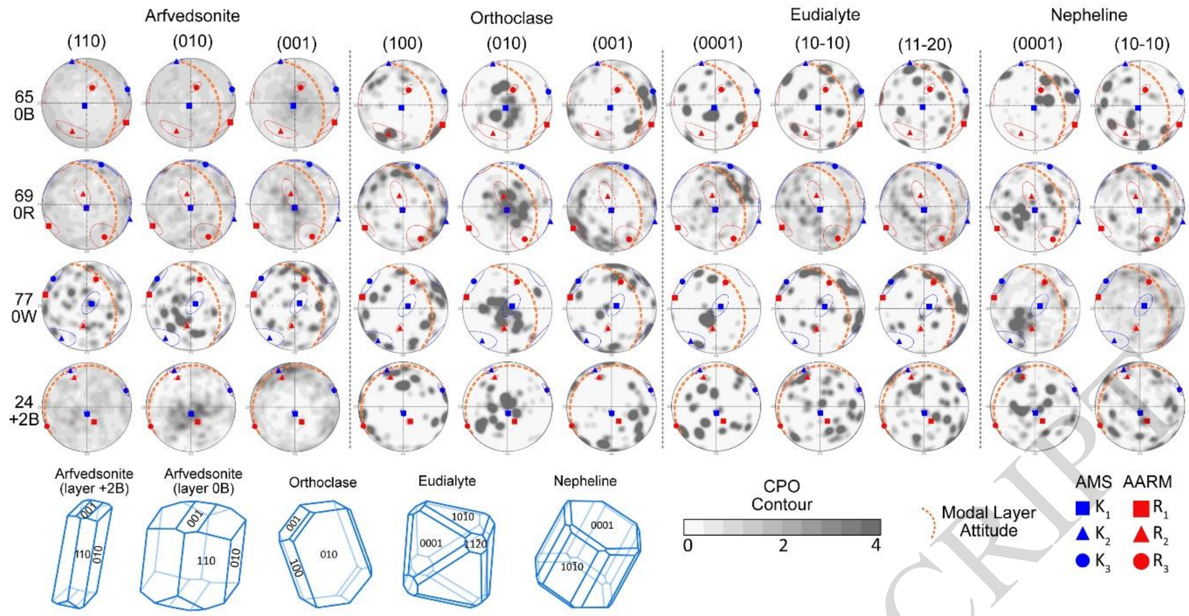
Arfvedsonite
(110)
(010)
(001)
Orthoclase
(100)
(010)
(001)
Eudialyte
(0001)
(10-10)
(11-20)
Nepheline
(0001)
(10-10)
65
0B
69
0R
77
0W
24
+2B
Arfvedsonite (layer +2B)
Arfvedsonite (layer 0B)
Orthoclase
Eudialyte
Nepheline
CPO Contour
0
2
4
Modal Layer Attitude
AMS
AARM
K1
K2
K3
R1
R2
R3

Figure 12

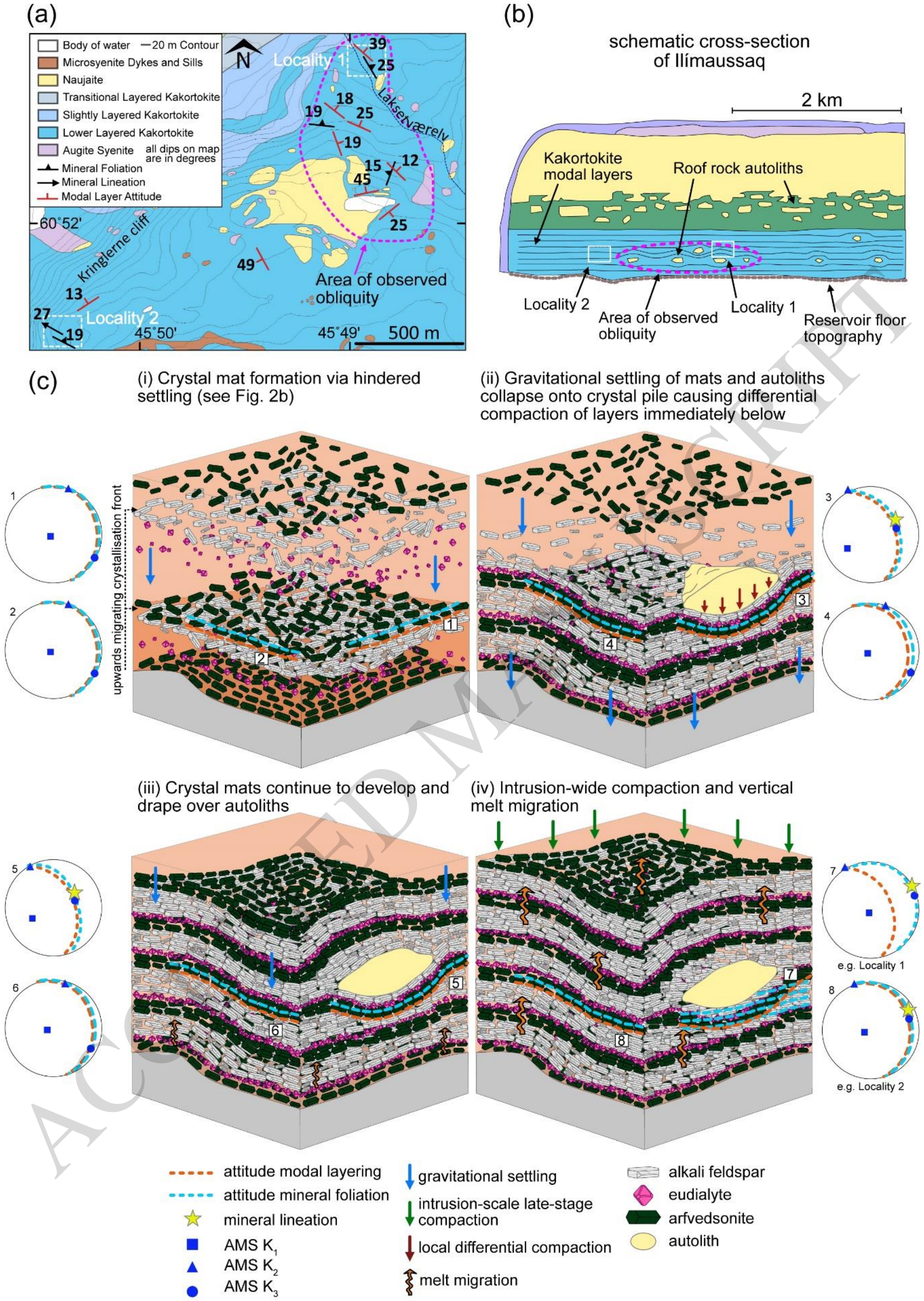

(a)
Body of water
20 m Contour
Microsyenite Dykes and Sills
Naujaite
Transitional Layered Kakortokite
Slightly Layered Kakortokite
Lower Layered Kakortokite
Augite Syenite
all dips on map are in degrees
Mineral Foliation
Mineral Lineation
Modal Layer Attitude
N
Locality 1
Laksetværelv
Kringlerne cliff
Area of observed obliquity
Locality 2
60°52'
45°50'
45°49'
500 m
(b)
schematic cross-section of Ilímaussaq
2 km
Kakortokite modal layers
Roof rock autoliths
Locality 2
Area of observed obliquity
Locality 1
Reservoir floor topography
(c)
(i) Crystal mat formation via hindered settling (see Fig. 2b)
(ii) Gravitational settling of mats and autoliths collapse onto crystal pile causing differential compaction of layers immediately below
upwards migrating crystallisation front
(iii) Crystal mats continue to develop and drape over autoliths
(iv) Intrusion-wide compaction and vertical melt migration
e.g. Locality 1
e.g. Locality 2
attitude modal layering
attitude mineral foliation
mineral lineation
AMS K_1
AMS K_2
AMS K_3
gravitational settling
intrusion-scale late-stage compaction
local differential compaction
melt migration
alkali feldspar
eudialyte
arfvedsonite
autolith

Figure 13